JGR Space Physics

RESEARCH ARTICLE
10.1029/2025JA034098

Special Collection:
Coupling Processes from Space to Earth

Stability of the Earth's Dayside Magnetosheath: Effects of Upstream Solar Wind Structures and Downstream Jets

Florian Koller[1,2], Cyril Simon Wedlund[1,3], Manuela Temmer[1], Ida Svenningsson[4,5], Luis Preisser[3,6], Adrian Pöppelwerth[7], Pauline A. Simon[2], Zoltán Vörös[3,8], Christopher H. K. Chen[2], Owen W. Roberts[9], and Ferdinand Plaschke[7]

[1]Institute of Physics, University of Graz, Universitätsplatz 5, Graz, Austria, [2]Department of Physics and Astronomy, Queen Mary University of London, London, UK, [3]Space Research Institute, Austrian Academy of Sciences, Graz, Austria, [4]Swedish Institute of Space Physics, Uppsala, Sweden, [5]Department of Physics and Astronomy, Uppsala University, Uppsala, Sweden, [6]LPC2E/CNRS, Orléans, France, [7]Institut für Geophysik und extraterrestrische Physik, TU Braunschweig, Braunschweig, Germany, [8]Institute of Earth Physics and Space Science, HUN-REN, Sopron, Hungary, [9]Department of Physics, Aberystwyth University, Aberystwyth, UK

Abstract The constant stream of plasma from the Sun, the solar wind, forms a bow shock as it interacts with Earth's magnetic field. The plasma properties change drastically as it crosses the shock and enter the downstream magnetosheath. This extended region hosts various kinetic ion plasma instabilities, such as mirror modes, ion cyclotron waves, and firehose instabilities, which develop due to local temperature anisotropies induced in the plasma. We use THEMIS satellite measurements from 2008–2023 combined with OMNI solar wind data to present the largest, to date, statistical analysis of temperature anisotropy-driven plasma instabilities in the dayside magnetosheath. We separate the magnetosheath into quasi-parallel and quasi-perpendicular regions and into the region close to the bow shock and close to the magnetopause, revealing fundamentally different plasma stability conditions in each region. The plasma conditions appear mostly stable, in particular in the quasi-parallel magnetosheath. There are nonetheless substantial populations beyond classical instability thresholds at increased temperature anisotropy, primarily occurring near the magnetopause and downstream of the quasi-perpendicular shock. Additionally, we show for the first time how impacting upstream solar wind structures alter parameters relevant for plasma stability in Earth's magnetosheath, revealing that coronal mass ejections cause the most extreme departure from nominal distributions. We apply our analysis to dynamic pressure enhancements known as magnetosheath jets. We find the plasma inside jets to be typically more stable to ion plasma instabilities. The plasma stability inside jets however is dependent on the choice of jet criteria, hinting at different jet sub-types being at play.

Plain Language Summary The Sun causes a constant outflow of charged particles. When those hit Earth's magnetic field, they get abruptly decelerated and deflected, creating a shock. This deceleration can cause the particle flow to become unstable. This means that highly fluctuating waves get created. The cause for these instabilities are pressure differences along and perpendicular to the magnetic field lines. Here we show the distribution of conditions that causes these instabilities at Earth's shock. We also demonstrate how the behavior of the region downstream of the shock, called the magnetosheath, changes when fast solar flow or magnetic clouds hit the system. Magnetic clouds cause the largest departure from nominal conditions. We then apply this analysis to a specific type of magnetosheath structure: we check the instability behavior of pressure enhancements, known as jets, behind Earth's shock. The analysis shows that these jets are predominantly stable with respect to the main wave modes present in the magnetosheath.

Key Points:

- We show how the global plasma stability differs in different regions of the terrestrial magnetosheath
- Solar wind structures change the magnetosheath plasma distributions, with Coronal mass ejections causing the most extreme departures from nominal conditions
- High-speed magnetosheath jets appear more often in the stable and firehose unstable regime compared to their surroundings

Correspondence to:
F. Koller,
f.koller@qmul.ac.uk

Citation:
Koller, F., Wedlund, C. S., Temmer, M., Svenningsson, I., Preisser, L., Pöppelwerth, A., et al. (2025). Stability of the Earth's dayside magnetosheath: Effects of upstream solar wind structures and downstream jets. *Journal of Geophysical Research: Space Physics*, *130*, e2025JA034098. https://doi.org/10.1029/2025JA034098

Received 18 APR 2025
Accepted 6 AUG 2025

Author Contributions:
Conceptualization: Florian Koller, Cyril Simon Wedlund, Manuela Temmer, Zoltán Vörös
Data curation: Florian Koller
Formal analysis: Florian Koller
Funding acquisition: Christopher H. K. Chen, Ferdinand Plaschke
Investigation: Florian Koller, Cyril Simon Wedlund
Methodology: Florian Koller, Cyril Simon Wedlund, Manuela Temmer, Ida Svenningsson, Luis Preisser, Adrian Pöppelwerth, Zoltán Vörös, Owen W. Roberts, Ferdinand Plaschke

1. Introduction

The Earth's magnetic field serves as an obstacle to the incoming, supermagnetosonic solar wind. The sudden deceleration at this obstacle causes the formation of the bow shock and a region with strongly varying plasma conditions downstream of it, called the magnetosheath. Shocks with supercritical Mach numbers cause plasma particles to get accelerated back sunwards along magnetic field lines, given that the orientation of the interplanetary magnetic field (IMF) allows it (Treumann, 2009). The angle between the shock normal and the IMF, θ_{Bn}, divides the shock into two qualitatively different global regions: quasi-parallel ($\theta_{Bn} < 45°$) and quasi-perpendicular ($\theta_{Bn} > 45°$). The interaction of the sunward-reflected particles with the incoming solar

Project administration: Zoltán Vörös, Owen W. Roberts, Ferdinand Plaschke
Software: Florian Koller, Ida Svenningsson, Adrian Pöppelwerth
Supervision: Manuela Temmer, Christopher H. K. Chen
Validation: Florian Koller, Christopher H. K. Chen, Owen W. Roberts
Visualization: Florian Koller, Cyril Simon Wedlund, Pauline A. Simon
Writing – original draft: Florian Koller, Cyril Simon Wedlund
Writing – review & editing: Florian Koller, Cyril Simon Wedlund, Manuela Temmer, Ida Svenningsson, Luis Preisser, Adrian Pöppelwerth, Pauline A. Simon, Zoltán Vörös, Christopher H. K. Chen, Owen W. Roberts, Ferdinand Plaschke

wind creates a turbulent region ahead of the quasi-parallel shock with a wealth of electromagnetic waves and structures—called the ion foreshock (Eastwood et al., 2005). Due to the upstream presence of the foreshock, the downstream quasi-parallel magnetosheath behaves differently in terms of produced turbulence and plasma instabilities compared to the quasi-perpendicular magnetosheath.

The magnetosheath is home to a variety of electromagnetic waves, structures, and transients. Departure of the plasma from a Maxwellian velocity distribution can create a local ion temperature (or pressure) anisotropy (Matteini et al., 2012), defined as the ratio between the ion temperatures parallel and perpendicular to the magnetic field, herein denoted as $A = T_{\perp}/T_{\parallel}$. Such an anisotropy can drive instabilities in the plasma by providing the necessary free energy to feed electromagnetic fluctuations (Gary, 1992). These fluctuations act to reduce the anisotropy, redistributing energy within the plasma and relaxing it toward local thermodynamic equilibrium conditions. Thus, temperature-anisotropy driven instabilities are associated to wave-particle and wave-wave interactions, changing plasma parameters in the process (Bandyopadhyay et al., 2022; Verscharen et al., 2019). The ion cyclotron and mirror mode instabilities are associated with a higher perpendicular ion temperature ($A > 1$), while the parallel and oblique firehose instabilities are connected to a higher parallel temperature ($A < 1$) (Verscharen et al., 2019). A competition takes place between these instabilities as they co-exist in a plasma, with the plasma beta playing the role of the arbiter (Hellinger et al., 2006). In a plasma with large A the mirror mode instability grows faster than the ion cyclotron instability for large plasma betas. In a plasma with small A, the oblique firehose instability growth rates tend to be larger than those of the parallel firehose instability for high plasma betas. We consider plasma to be stable if it doesn't fall in either of these conditions, which is the case for $A \sim 1$.

Temperature anisotropy sources in the Earth's magnetosheath are linked to compression at the shock on the one hand and the magnetopause boundary on the other due to the conservation of the adiabatic invariants (Anderson & Fuselier, 1993; Chao et al., 1995; Crooker & Siscoe, 1977; Schwartz et al., 1996). Quasi-perpendicular shocks are the source of plasma heating preferentially in the perpendicular direction to the background magnetic field, causing an increase in A (Balogh & Treumann, 2013). Thus, the plasma downstream of the quasi-perpendicular bow shock (i.e., the quasi-perpendicular magnetosheath) shows an increase of mirror mode and ion cyclotron wave activity. In contrast, the quasi-parallel magnetosheath is expected to show a low A (Dimmock et al., 2015; Yordanova et al., 2020). This region however shows numerous transient structures due to the upstream foreshock, acting as a source of coherent fluctuations, waves, and intermittency that are continuously processed by the bow shock (Gurchumelia et al., 2022). Close to the magnetopause (in either magnetosheath region), the plasma depletion layer causes increased values in A (Anderson & Fuselier, 1993; Phan et al., 1994; Soucek et al., 2015). In view of these differences in the magnetosheath characteristics, the analysis of plasma stability in the magnetosheath requires a differentiation into quasi-parallel and quasi-perpendicular regions, as well as regions close to the bow shock and close to the magnetopause.

The incoming solar wind is responsible for shaping the magnetosheath: the IMF orientation dictates magnetic shock geometry, and the solar wind Mach number determines the shock strength. Both parameters in turn influence the plasma upstream (e.g., foreshock structure formation, Xirogiannopoulou et al., 2024; H. Zhang et al., 2022) and downstream of the shock. Additionally, the solar wind itself is not uniform on large scales (both temporal and spatial), and different large-scale structures can emerge within it. Fast solar wind originate from coronal holes (high-speed streams (HSSs)) and typically show lower density and higher plasma temperature in addition to the increased velocity. Coronal mass ejections (CMEs) can emerge from the solar corona as coherent magnetic structures that move through interplanetary space (e.g., Temmer, 2021). The inner part of CMEs consist of a flux rope with a rotating magnetic field vector. We will refer to this magnetic structure as the magnetic ejecta (CME-ME). Fast CMEs can drive an interplanetary shock and a sheath region in front of the ME, which we will denote as CME-SH. This region can also harbor instabilities such as mirror mode waves similar to planetary bow shocks (Ala-Lahti et al., 2018; Liu et al., 2006; Pitňa et al., 2021; Shaikh et al., 2023). Solar wind characteristics change and restrict the possible plasma parameter space when it hits near-Earth space (Koller et al., 2024). However, the dependence of terrestrial magnetosheath plasma instabilities on solar wind structures has not been explored so far.

Dynamic pressure enhancements (or so-called "Jets") are mesoscale structures that mostly appear in the quasi-parallel magnetosheath (Krämer et al., 2025; Plaschke et al., 2018, and references therein), though a residual population can occur in the quasi-perpendicular magnetosheath and in the boundary between both (Goncharov

et al., 2020; Kajdič et al., 2021; Raptis et al., 2020; Vuorinen, LaMoury, et al., 2023). The formation of the majority of these jets is connected to foreshock effects such as shock rippling (Hietala et al., 2009; Preisser, Blanco-Cano, Kajdič, et al., 2020), shock reformation (Raptis, Karlsson, Vaivads, Pollock, et al., 2022) or upstream compressional structures in the foreshock (Suni et al., 2021, 2023; Xirogiannopoulou et al., 2024). A subset of jets was also reported at the quasi-perpendicular shock transition layer (Vuorinen, LaMoury, et al., 2023). Several works investigated the influence of solar wind parameters (Goncharov et al., 2020; LaMoury et al., 2021; Plaschke et al., 2013; Vuorinen et al., 2019), solar wind structures (Koller et al., 2022, 2023), and, consequently, the solar activity cycle influence on jets (Vuorinen, LaMoury, et al., 2023). Some jets appear simultaneously with mirror mode waves as well (Blanco-Cano et al., 2020, 2023). Recently, the first statistical analysis of stability in jets by Osmane and Raptis (2024) showed mostly stable conditions with departures from stability being common. We expand on this analysis with a larger data set and employing the differentiation into the different magnetosheath regions. Notably, there are different criteria that define jets (Plaschke et al., 2018, and references therein), two of which will be employed in this work.

Overall, only a small number of studies have so far been conducted on the global analysis of instabilities in magnetosheath plasma (Artemyev et al., 2022; DeWeese et al., 2022; Dimmock et al., 2015; Jiang et al., 2025; Lewis et al., 2024; Maruca et al., 2018; Shaikh et al., 2023; Soucek et al., 2015; Svenningsson et al., 2024). In contrast to some of these recent works which often focus on intervals of turbulent fluctuations in Earth's magnetosheath, our results showcase the total overall plasma behavior in the magnetosheath.

The aim of this work is threefold:

- Provide the largest possible statistical overview of dayside magnetosheath plasma distribution with respect to ion instabilities. This will reveal the general behavior of the plasma and its dependence on the position in the magnetosheath.
- Show how this distribution is changed and impacted by upstream solar wind structures. How the magnetosheath alters incoming solar wind structures (or vice-versa) via instabilities is inherently important to improve our understanding of solar wind–magnetosphere couplings especially during times of geomagnetic storms caused by CMEs or during HSSs.
- Demonstrate where magnetosheath jets fall into these distributions in order to further understand their formation and behavior as they move through the magnetosheath.

This work gives additional context and expands on the studies of Soucek et al. (2015) and Jiang et al. (2025), who used 2 years of Cluster II mission observations (Escoubet et al., 1997) and 4 years of Magnetospheric Multiscale mission (MMS) (Burch et al., 2016) burst data, respectively, to analyze plasma stability and in the terrestrial magnetosheath as a function of spacecraft location and upstream parameters. In contrast to their work, we use 16 years of THEMIS observations, which enables us to statistically connect to large-scale solar wind transients like HSSs and CMEs.

2. Data and Methods

2.1. Solar Wind and Magnetosheath Intervals

We require data sets spanning more than one solar cycle. Therefore we use data from the Time History of Events and Macroscale Interactions during Substorms (THEMIS) mission (Angelopoulos, 2008) from January 2008 to the end of December 2023. We use corresponding upstream solar wind values by OMNI (King & Papitashvili, 2005). The electrostatic analyzer (ESA, McFadden et al., 2008) and the fluxgate magnetometer (FGM, Auster et al., 2008) on THEMIS provide data for ion moments and magnetic fields. The definition of subsolar magnetosheath intervals follows Koller et al. (2023) and Plaschke et al. (2013): the plasma density is required to exceed twice the corresponding OMNI solar wind density. The spacecraft positions are restricted to a distance of 7–18 Earth radii (R_e) and have to be within a cone of 30° angle surrounding the Sun-Earth line, with the tip of the cone at Earth's center. Additionally, the 10-keV ion energy flux is required to be less than the 1-keV ion energy flux to remove intervals of magnetospheric plasma (Plaschke et al., 2013). Magnetosheath intervals of 1 min or longer are considered. We use the geocentric solar ecliptic system (GSE), which has its GSE-X axis pointing from the Earth to the Sun, the GSE-Y axis pointing duskward in the ecliptic plane, and the GSE-Z axis pointing perpendicularly to the ecliptic.

We use the reduced ion moment data products of ESA and the FGS data product of FGM, both providing 3-s, spin-resolution data. Similar to the study by Soucek et al. (2015), the ESA instrument does not separate ion species, thus contamination by alpha particles is likely. The alpha particle abundance is usually low in comparison to the proton abundance (2%–5% in the solar wind depending on the solar wind origin, speed, and cycle, see Alterman & Kasper, 2019; Kasper et al., 2007; Xu & Borovsky, 2015), thus we assume the ion moments to be an acceptable approximation of the proton moments. The ion data products of $T_\perp$ and $T_\parallel$ were cross-checked by explicitly calculating both quantities based on the full pressure tensor provided by the ESA instrument, with agreeing results. The parallel ion plasma beta is defined by $\beta_\parallel = \frac{2\mu_0 n_i k_B T_\parallel}{|B|^2}$, with μ_0 being the vacuum magnetic permeability, n_i the ion number density, k_B the Boltzmann constant, and $|B|$ the total magnetic field strength. The ion dynamic pressure is defined as $p_{\mathrm{dyn}} = 0.5\rho v^2$, with ρ the ion density and v the ion plasma bulk speed.

2.2. Structured Solar Wind and Jet Lists

Solar wind structure lists for HSSs, CME-MEs, and CME-SH are provided by the work of Koller et al. (2023) and were extended until the end of 2023 (see Koller (2025) for the stream interaction region list which includes the HSSs and Richardson and Cane (2010) for the CME events). We utilize two different criteria to identify jets. First we use the definition as in Plaschke et al. (2013) where jets are defined by structures fulfilling: $p_{\mathrm{dyn,\,X}} > \frac{1}{2} p_{\mathrm{dyn,X,sw}}$, where $p_{\mathrm{dyn,X}}$ denotes the dynamic pressure in GSE-X direction, and $p_{\mathrm{dyn,X,sw}}$ the dynamic pressure of the solar wind obtained by OMNI. The ion GSE-X velocity is required to be negative (earthward), and the magnetosheath GSE-X velocity within 1 min before and after the jet interval is required to go above half of the measured GSE-X velocity at the time of the $p_{\mathrm{dyn,X}}$ peak. The jet duration is defined as the range when $p_{\mathrm{dyn,X}}$ exceeds 1/4 of the dynamic pressure in the solar wind. These thresholds reduce the jet duration to p_{dyn} increases that go beyond expected values downstream of the subsolar shock using Rankine-Hugoniot relations (Hietala et al., 2012, 2024). The second jet criterion we use is defined by Archer and Horbury (2013) as $p_{\mathrm{dyn}} > 2\langle p_{\mathrm{dyn}} \rangle_{20\mathrm{min}}$, where $\langle p_{\mathrm{dyn}} \rangle_{20\mathrm{min}}$ denotes the 20-min average dynamic pressure of the magnetosheath. Notably, this is less restrictive than the Plaschke et al. (2013) criterion. For both criteria only jets that surpass a duration of 10 s and are shorter than 300 s are included (limiting to events with more than 3 measured data points and excluding events that are larger than the magnetosheath thickness). All magnetosheath and jet intervals are available in Koller (2025), totaling 405.0 days of available THEMIS magnetosheath measurements. Within this time, we have 73.9 days of HSSs data, 26.1 days of CME-ME data, and 8.4 days of CME-SH data within the terrestrial magnetosheath. We have 10,478 jets following the Plaschke et al. (2013) criterion and 14,083 jets following the Archer and Horbury (2013) criterion.

2.3. Dividing Magnetosheath Regions

We divide the magnetosheath measurements into categories based on their spatial position (close to the bow shock or close to the magnetopause) and the region (quasi-parallel or quasi-perpendicular). The relative spacecraft position F within the magnetosheath, where $F = 0$ corresponds to the magnetopause and $F = 1$ corresponds to the bow shock, is derived using the bow shock distance and shape by Merka et al. (2003) and the magnetopause model by Shue et al. (1998). Both models use the current OMNI solar wind parameters as input. To keep radial distance uncertainties to a minimum, we restrict the data to locations close the bow shock ($F > 0.66$) and close to the magnetopause ($F < 0.33$). We estimate θ_{Bn} using the OMNI IMF vector and the normal of the modeled bow shock. This value determines the region of the magnetosheath. During intermediate values of θ_{Bn}, the magnetosheath can display traits typical for either both quasi-parallel or quasi-perpendicular geometries depending on foreshock boundary location (Karlsson et al., 2021; Svenningsson et al., 2025). Therefore, we require $\theta_{\mathrm{Bn}} > 60°$ for the quasi-perpendicular and $\theta_{\mathrm{Bn}} < 30°$ for the quasi-parallel magnetosheath. In addition, we require the ESA ion energy flux in the highest 3 bins to exceed pre-defined thresholds to strengthen the robustness of matching the correct plasma environment (following Karlsson et al., 2021; Koller et al., 2024). The technical aspects of the methods are described in Appendix A and Appendix B. Table 1 shows the total number of data points, jets, and equivalent amount of measurement time after dividing the measurements into the four categories.

2.4. Analysis in the A–$\beta_\parallel$ Plane

To analyze the plasma stability of protons, the threshold conditions are given in the following form (Hellinger et al., 2006; Verscharen et al., 2019):

Table 1
Number of Data Points, Number of Jets, and Equivalent Time Duration of Measurements for Each of the Defined Magnetosheath Region

Data/Region	Qpara near BS	Qperp near BS	Qpara near MP	Qperp near MP	Total
Total	7,754 pts	753,446 pts	622,387 pts	1,643,834 pts	3,097,207 pts
	64.6 hr	627.9 hr	518.7 hr	1,369.9 hr	2,581.0 hr
HSS	20,375 pts	161,929 pts	113,067 pts	260,190 pts	555,561 pts
	17.0 hr	134.9 hr	94.2 hr	216.8 hr	463.0 hr
CME-ME	4,647 pts	80,684 pts	24,766 pts	165,064 pts	275,161 pts
	3.9 hr	67.2 hr	20.6 hr	137.6 hr	229.3 hr
CME-SH	184 pts	17,761 pts	9,282 pts	18,739 pts	45,966 pts
	0.2 hr	14.8 hr	7.7 hr	15.6 hr	38.3 hr
Jet (Plaschke)	296 Jets	167 Jets	1,230 Jets	48 Jets	1,841 Jets
	2.5 hr	1.5 hr	5.6 hr	0.3 hr	9.9 hr
Jet (Archer)	68 Jets	140 Jets	1,847 Jets	552 Jets	2,607 Jets
	0.4 hr	1.0 hr	4.9 hr	1.3 hr	7.6 hr

$$A = 1 + \frac{a}{\left(\beta_{\parallel} - \beta_0\right)^b}, \tag{1}$$

where a, b, and β_0 are fitted parameters for each instability (proton-cyclotron, mirror mode, parallel firehose, oblique firehose), and $\beta_{\parallel}$ denotes the parallel proton plasma beta. The constants are taken from Verscharen et al. (2016) based on a $10^{-2}\ \Omega_p$ growth rate, where Ω_p is the proton cyclotron frequency. We explore the effects of lower growth rates on the analysis in Section 4.2. In this work we implicitly consider the values for protons only, while Equation 1 is valid for any type of ion species. Unstable plasma will relax back to equilibrium, stable conditions by wave-wave and wave-particle interactions, coming closer and closer to the respective instability threshold defined by Equation 1 (Hellinger et al., 2006, 2019). Plotting plasma properties as bi-variate (two-dimensional) histograms in the A–$\beta_{\parallel}$ plane, a representation sometimes called "Brazil plots" due to the distribution seen in the solar wind, is a useful tool to compare plasma properties with the typical linear plasma instability thresholds (Verscharen et al., 2019). In this plane, each measured point will fall into a specific bin of the histogram. Throughout this work, we will refer to the plasma distribution within this plane to describe the plasma behavior with respect to the common plasma instabilities. We note that this analysis provides a general overview, while individual cases require a closer look at polarization properties to infer, whether an instability was triggered.

3. Results

The full distribution of magnetosheath plasma in the A–$\beta_{\parallel}$ plane is shown in Figures 1a and 1b as bi-variate histograms of the THEMIS data set. The sketch on the top indicates the stable and unstable parameter conditions, separated by the proton instability thresholds. The upper, solid line shows the ion cyclotron and the upper, dashed line the mirror mode instability threshold. We defined the plasma above each of these lines to be unstable to the respective instability. We count plasma in the overlapping areas toward the mirror mode instability because it mostly covers high β values, which favor mirror mode over ion cyclotron instabilities. The lower, solid line shows the parallel firehose, and the lower, dashed line the oblique firehose instability threshold. Plasma below each of these lines is unstable to the respective instability. Figure 1a shows the full bi-variate histogram distribution in number of data points per bin. Figure 1b shows the probability density of all measurements following Maruca et al. (2018) defined by $n_{\mathrm{bin}}/(n_{\mathrm{tot}}\Delta\beta_{\parallel}\Delta A)$, with n_{bin} being the data points per bin, and n_{tot} the total number of data points of all four panels. This accounts for the logarithmically spaced X and Y axis bins. The plots show a grid of 50×50, covering ranges of $0.5 < A < 5$ and $0.005 < \beta_{\parallel} < 150$. Bins with less than 10 data points are omitted. Using the growth rate of $10^{-2}\ \Omega_p$ for the thresholds, the majority (72.8%) of the plasma is within the stable regime, matching previous results (Jiang et al., 2025; Maruca et al., 2018). There is a significant amount of measurements

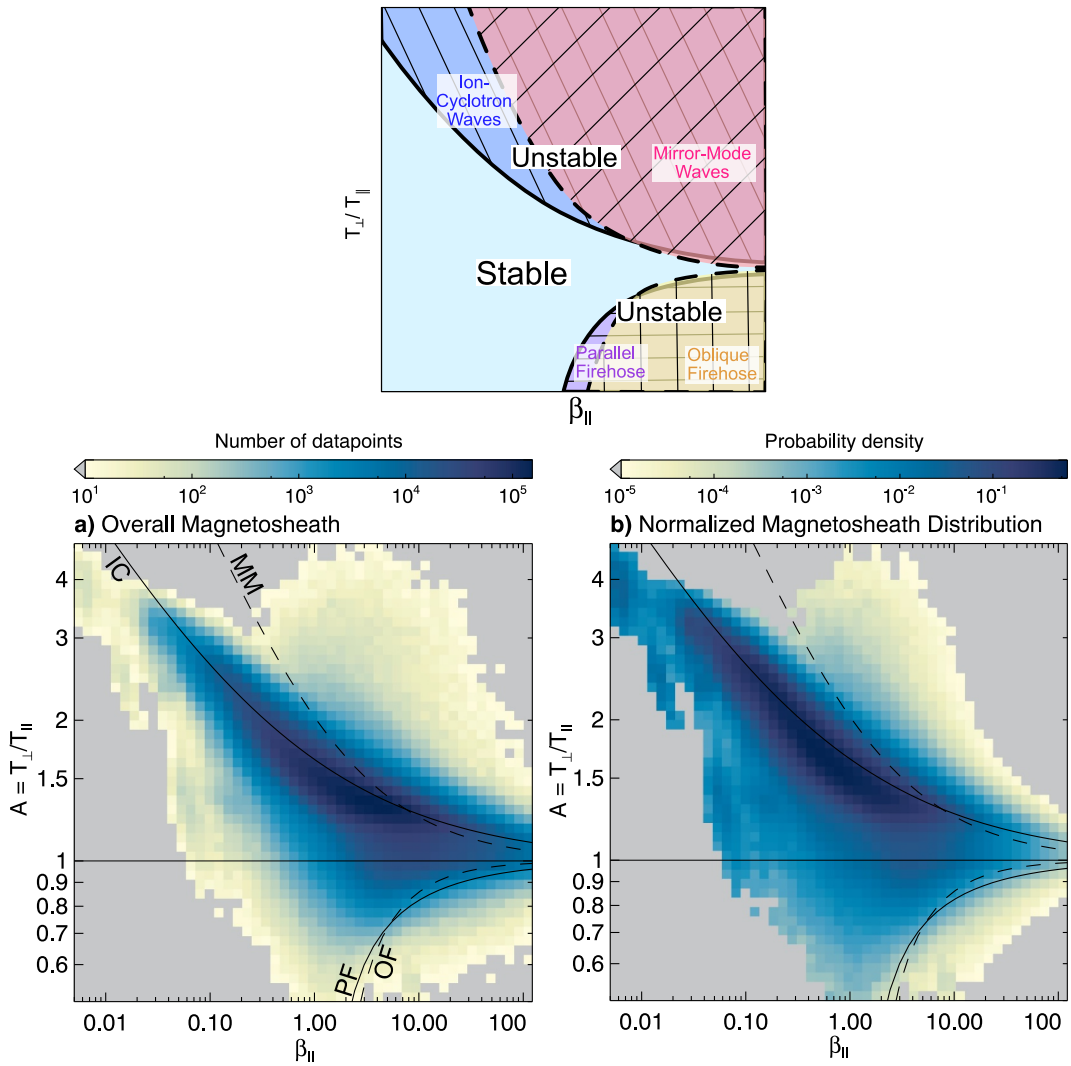

Figure 1. 2D bi-variate histograms showing the magnetosheath plasma distribution in the A–$\beta_{\parallel}$ plane in log-log scale. The top panel shows a sketch of the stable and unstable regions of protons in the plot. (a) General distribution of all number of data points, with 30 being the lowest shown value. (b) Probability density of all measurements following Maruca et al. (2018). Overlaid on all plots are the proton instability thresholds based on Verscharen et al. (2016) using a growth rate of 0.01 Ω_{cp}.

in the defined regimes unstable to the ion cyclotron (19.3%) and mirror mode (6.9%) instabilities. Only a minor portion of the measurements in our study appears to be in the regime unstable to the firehose instabilities (1.0%). For the subsequent plasma distribution in each spatial region of the magnetosheath we will use the probability density measure given in Figure 1b.

3.1. Change in Distributions Due To Location in the Magnetosheath

Figure 2 shows the distribution of magnetosheath plasma in the A–$\beta_{\parallel}$ plane separated into four regions: (a) quasi-parallel magnetosheath near the bow shock, (b) quasi-perpendicular magnetosheath near the bow shock, (c) quasi-parallel magnetosheath near the magnetopause, and (d) quasi-perpendicular magnetosheath near the magnetopause. The grid resolution is 50×50, in the ranges $0.5 < A < 5$ and $0.005 < \beta_{\parallel} < 150$, with a minimum number of 10 points per bin. Figure 2 includes a dayside magnetosheath sketch to spatially allocate each region. The following analysis on the amount of measurements in stable and unstable regimes is based on the growth rate of $10^{-2}\,\Omega_p$, while we discuss lower growth rates in Section 4.2. As evidenced in Figure 2a, the plasma just downstream of the quasi-parallel bow shock is primarily in stable conditions (84%), with 4.8% and 4.2% of the

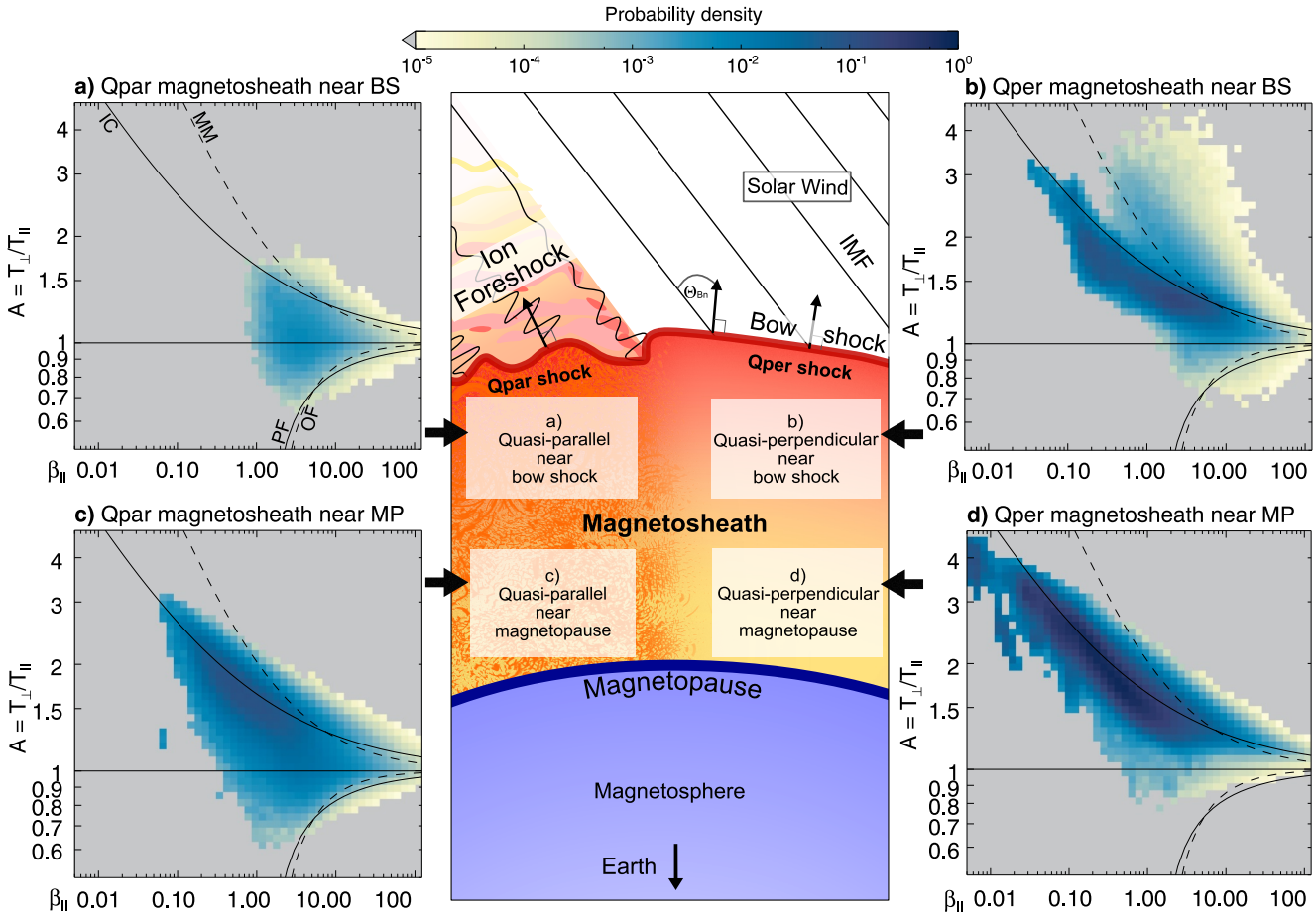

Figure 2. Sketch of the dayside magnetosheath and statistical plasma distributions of A versus $\beta_{\parallel}$ in four different magnetosheath regions. The normalization and instability thresholds are the same as in Figure 1b. Each box in the middle sketch represents the spacecraft location for the distribution in panels (a–d), as indicated with the black arrows.

plasma being in the defined ion cyclotron and mirror mode instability regimes, respectively. The median $\beta_{\parallel}$ is 7.04 and the plasma is primarily isotropic (median of $A = 1.04$). In comparison, the plasma just downstream of the quasi-perpendicular bow shock (Figure 2b) shows overlapping subpopulations: one with a distribution peaking just below the ion-cyclotron instability threshold and one well above the mirror mode instability threshold. Both populations have high A values as expected for this shock geometry and reach lower $\beta_{\parallel}$ values compared to their quasi-parallel counterpart, possibly owing to the magnetic field strength asymmetry in the magnetosheath under Parker-spiral conditions (Walsh et al., 2012). The population well above the mirror mode instability appears to be uniquely associated with the quasi-perpendicular shock transition layer after manually inspecting instances showing these conditions. We discuss this population in more detail in Section 4.1. Overall, Figure 2b shows 79.7% in the defined stable condition, with 10.9% and 9.0% of the plasma being unstable to the ion cyclotron and mirror mode instability, respectively. The median value of $A = 1.29$ is increased, while the median value of $\beta_{\parallel} = 4.16$ is lower compared to the quasi-parallel counterpart. There is a significant number of measurements below both defined firehose thresholds close to the bow shock (3.3% in the quasi-parallel magnetosheath, Figure 2a, and 0.3% in the quasi-perpendicular magnetosheath, Figure 2b). The anisotropy increases close to the magnetopause for both quasi-parallel (Figure 2c, median $A = 1.28$) and quasi-perpendicular (Figure 2d, median $A = 1.28$) regimes when compared to their close-to-the-bow-shock counterparts. $\beta_{\parallel}$ decreases likely due to the increment in magnetic field strength closer to the magnetopause (Dimmock & Nykyri, 2013), with a median value of $\beta_{\parallel} = 3.17$ in the quasi-parallel region (Figure 2c), and a median value of $\beta_{\parallel} = 1.13$ in the quasi-perpendicular region (Figure 2d). The anti-correlation of A and $\beta_{\parallel}$ close to the magnetopause is associated with the plasma depletion layer (Phan et al., 1994; Soucek et al., 2015). This general result matches with the conclusions of Soucek

et al. (2015): the median A in both their high θ_{Bn} and low θ_{Bn} bins increased close to the magnetopause (Figure 6a in Soucek et al., 2015), while the median β in general decreased (Figure 6d in Soucek et al., 2015). Figure 2c shows 74.3% in the defined stable condition, with 17.7%, 6.1%, and 1.1% of the plasma appearing within the defined regimes unstable to ion cyclotron, mirror mode, and oblique firehose instability, respectively. Figure 2d shows 66.0% in the defined stable condition, with 26.3% and 7.7% of the plasma appearing within the defined regimes unstable to ion cyclotron and mirror mode instability, respectively. The number of measurements in firehose unstable conditions is negligible in the latter case.

3.2. Change in Distributions Due To Solar Wind Structures

With the region-based magnetosheath distributions established, we now show how three distinct types of large-scale solar wind structures, namely HSSs, CME-MEs, and CME-SHs, change the general stability of Earth's magnetosheath plasma. The following plots show sub-populations of the bi-variate histograms shown in Figure 2. Figure 3 gives an overview of the magnetosheath plasma stability during HSSs following the same format as Figure 2. The grid resolution is reduced to 40 × 40, with a minimum of 10 points per bin. This solar wind condition, which is often denoted as the fast solar wind, corresponds to high plasma velocity, high temperature, and low density. Consequently, β in the magnetosheath is increased, and we see the majority of $\beta_{||}$ measurements close to the bow shock (Figures 3a and 3b) restricted to $\beta_{||} > 0.5$. HSSs are also the primary cause for the residual subpopulation of plasma with A around one or lower in the quasi-perpendicular region close to the magnetopause (as seen in Figure 2d).

The distribution of Earth's magnetosheath plasma during the passing of CME-MEs is given in Figure 4. The angle between the IMF and the Sun-Earth line inside CME-MEs is on average very high (Koller et al., 2023), which causes more instances of quasi-perpendicular measurements. High magnetic field strengths and low temperatures, typical of magnetic flux ropes of CMEs, result in low β values. This is particularly visible in Figures 4b and 4d. The combination of plasma parameters in CME-MEs often cause low Alfvén Mach numbers. The plasma downstream of low Alfvén Mach number shocks is known to be correlated to high A (Gary et al., 1993; Soucek et al., 2015). Considering the combination of all these conditions, CME-ME events are the cause for the most extreme low $\beta_{||}$ and high A values in the quasi-perpendicular sheath.

Figure 5 shows the magnetosheath plasma stability behavior during CME-SH passage, for which we have the lowest amount of data in this work. The parameter range is kept the same as in the previous plots, while the grid resolution is reduced to 30 × 30, with a minimum of 10 points per bin. CME-SHs are the downstream region of interplanetary shocks driven by CMEs. Therefore, the magnetosheath plasma analyzed here has been processed by two shocks: the CME-driven interplanetary shock and Earth's bow shock. CME-SHs show increased magnetic field strength, density, and statistically very high angle between the IMF and the Sun-Earth line (Koller et al., 2023). The resulting A is considerably increased, visible in Figures 5b and 5d.

The plasma stability in the quasi-parallel region behaves similarly between all three structures. Plasma is mostly bounded to the stable region near the bow shock and spreading out along the ion cyclotron threshold line closer to the magnetopause. Differences arise in the quasi-perpendicular region. HSSs cause a more diluted distribution spanning the defined stable, ion cyclotron instability, and mirror mode instability regimes (Figures 3b and 3d). This highlights the fact that detailed polarization analysis is required to infer the condition of fluctuations in these cases. In comparison, magnetosheath plasma in CME-ME and CME-SH events are primarily bounded by the ion-cyclotron threshold, rising up to high values of A (Figures 4b, 4d, 5b, and 5d). Additionally, the subpopulation of mirror mode unstable plasma close to the bow shock is more prevalent in HSSs (Figure 3b). Close to the magnetopause there is always a residual population in mirror-mode unstable conditions in all solar wind structures (when considering growth rate of $10^{-2}\ \Omega_p$ or lower). However, HSSs cause a higher percentage of mirror mode unstable plasma compared to the other structures in all four analyzed regions. HSSs also cause more incidents of plasma being in firehose unstable regimes compared to both CME-MEs and CME-SHs in all four regions.

3.3. Magnetosheath Jet Distribution

Based on the previous analysis we showcase an application for the study of plasma stability in magnetosheath jets using two different jet criteria. In contrast to the previous figures, Figure 6 shows the jet percentage in the four

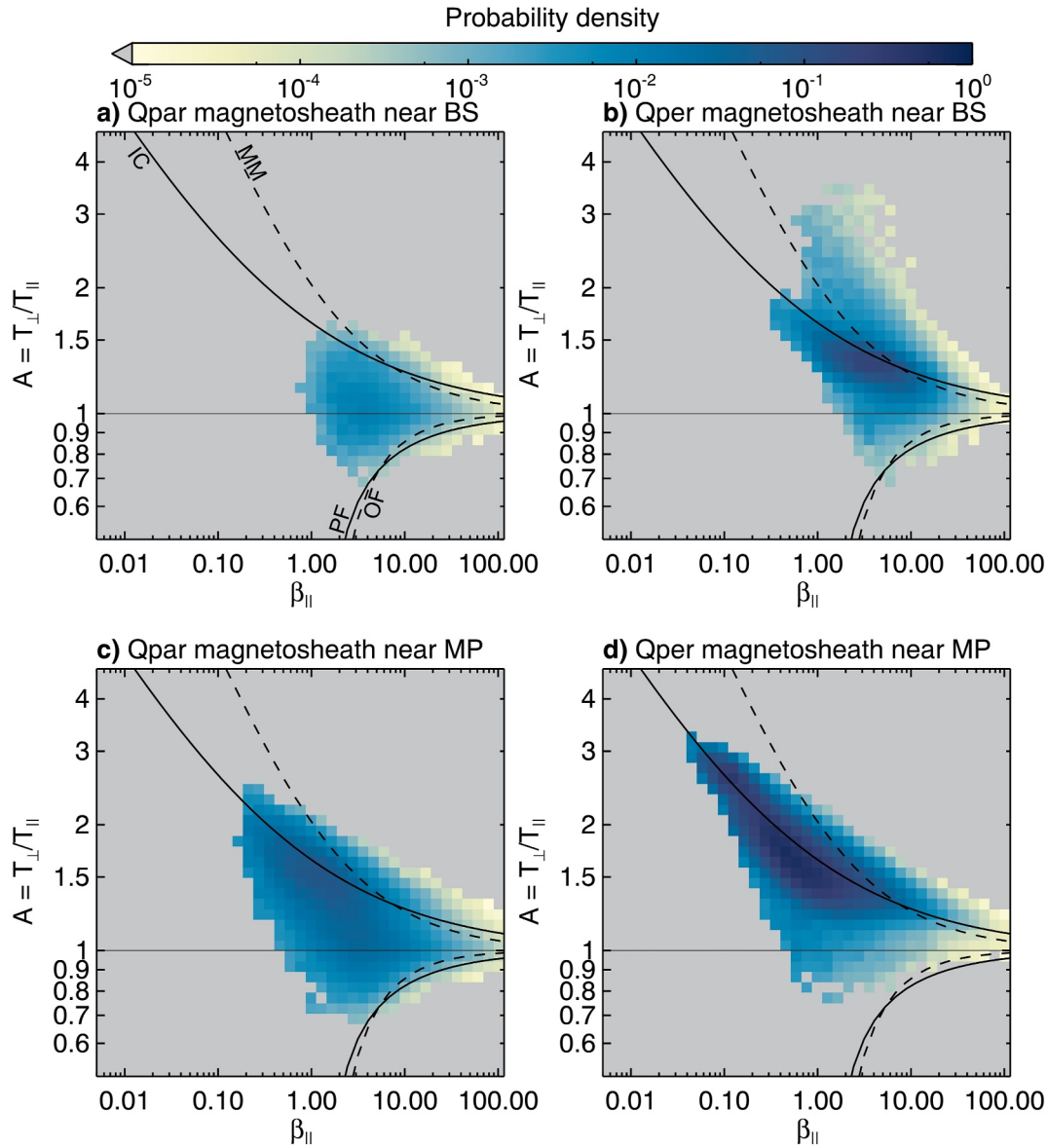

Figure 3. Dayside magnetosheath plasma distribution as in Figure 2 during high-speed stream conditions.

quadrant plots. The jet percentage per bin is defined by the number of data points within jet intervals divided by the total magnetosheath data points per bin. These jets are defined by the Plaschke et al. (2013) criterion. Only bins with at least one data point during a jet interval are given. The parameter range is $0.5 < A < 4$ and $0.05 < \beta_{||} < 150$ with a grid resolution of 30 × 30. The overlaid contours indicate the total time amount of background magnetosheath measurements (see Figure 2). In other words, the distributions show, how much percent of the total magnetosheath measurements in each region were measured during jet intervals.

A total of 89.3% of all jet measurements based on the Plaschke criterion fall into the stable plasma regime based on instability thresholds using a growth rate of $10^{-2}\,\Omega_p$. Most jets were detected in the quasi-parallel magnetosheath (Table 1). There is a population of jet measurements beyond the mirror mode threshold in the quasi-perpendicular magnetosheath near the bow shock (Figure 6b). These are likely connected to pressure enhancements resulting from gyro-bunched ions as part of the quasi-perpendicular shock transition layer as reported by Vuorinen, LaMoury, et al. (2023). The total number of measurements within jets appearing in the defined regime unstable to the mirror mode (20.9%) and in the defined ion-cyclotron instability regime (15.5%) close to the quasi-perpendicular bow shock decreases significantly close to the magnetopause (Figures 6d) to 2.0% and 8.0%,

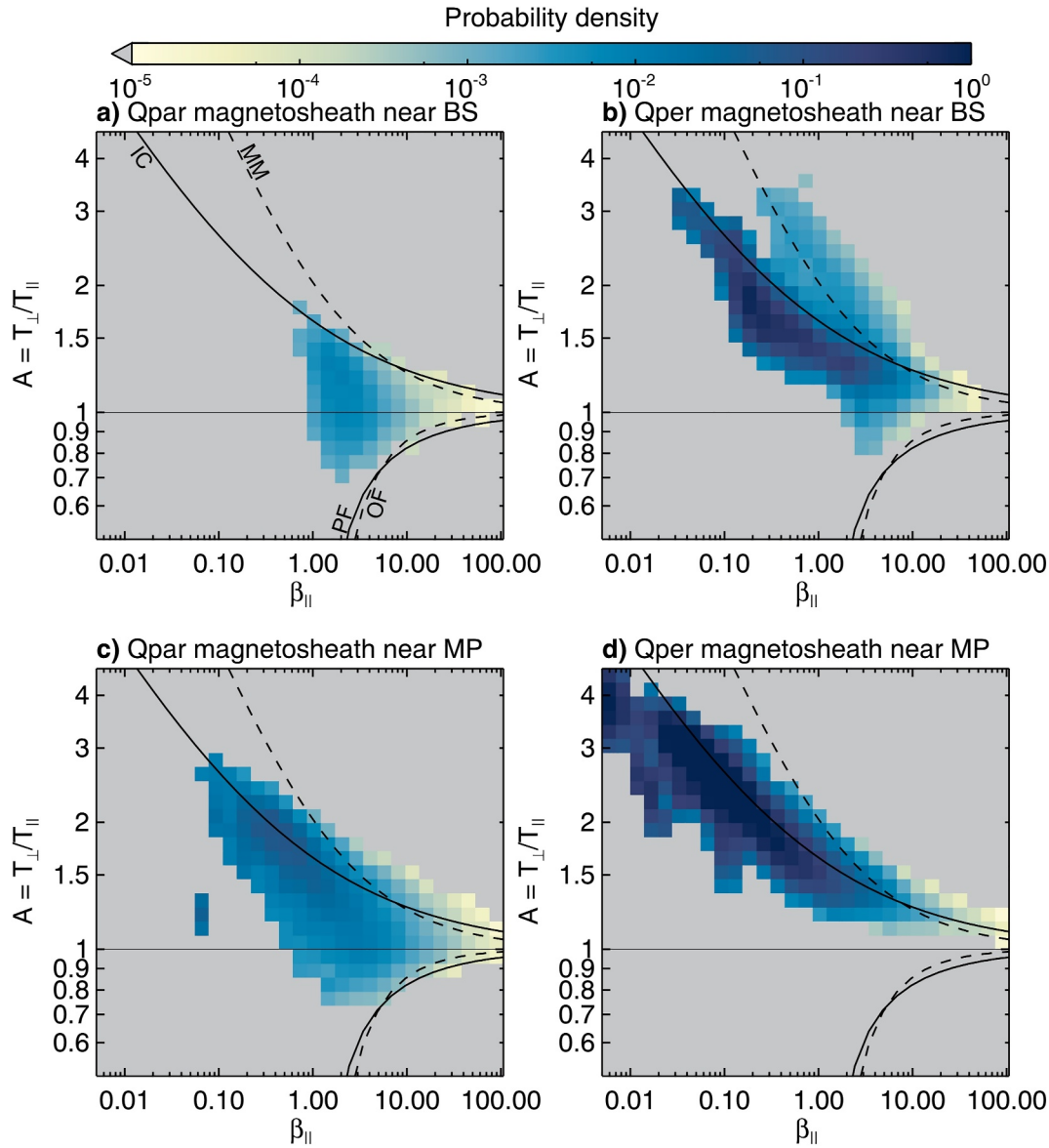

Figure 4. Dayside magnetosheath plasma distribution as in Figures 2 and 3 during coronal mass ejection - magnetic ejecta conditions.

respectively. About 1%–5% of jet measurements appear to be below the defined oblique or perpendicular firehose thresholds (Figures 6a–6c). Close to the magnetopause, the jet percentage increases toward lower values of A (Figures 6c and 6d). The detached population of measurements at low $\beta_{||}$ in Figure 6d is connected to short intervals during CMEs that briefly fulfilled the jet criterion.

Figure 7 shows jet measurements divided by the overall distribution per bin in each magnetosheath region using the same parameter range and resolution as in Figure 6 now using the jet criterion by Archer and Horbury (2013). There are significantly more jet intervals close to the magnetopause (Figures 7c and 7d) than to the bow shock. A few significant differences to the distribution based on the Plaschke et al. (2013) criterion are evident: Close to the magnetopause, we see more Archer criterion jet measurements being mirror-mode-unstable (Figures 7c and 7d) compared to Plaschke criterion jets (Figures 6c and 6d). The jet percentage of Archer criterion jet appears to increase beyond the mirror mode threshold toward the upper limit of available data (Figures 7c and 7d). Close to the quasi-perpendicular bow shock, the population of jets beyond the mirror-mode threshold is significantly smaller in the Archer criterion (Figure 7b compared to Figure 6b). A few instances of Archer criterion jets are in

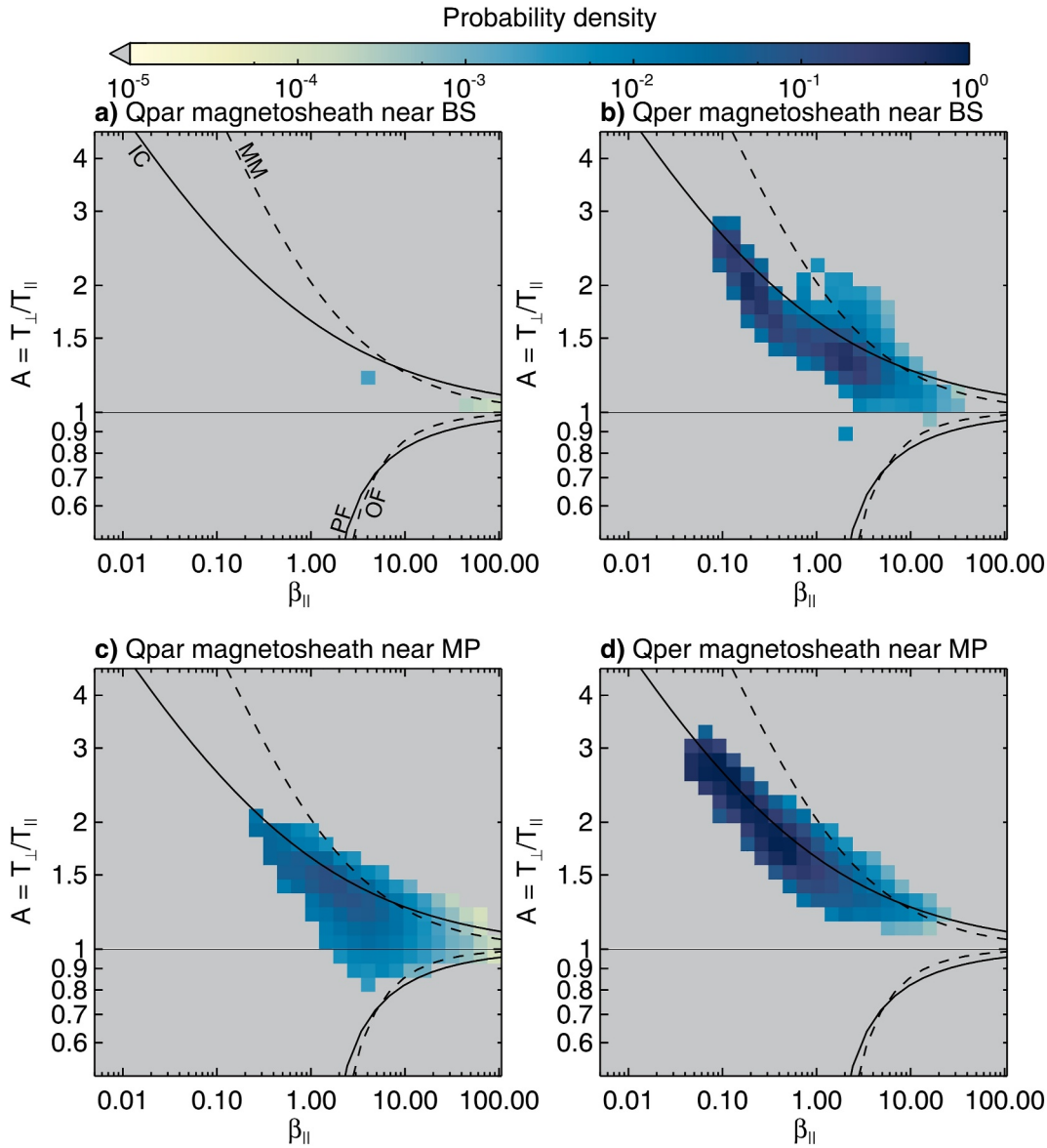

Figure 5. Dayside magnetosheath plasma distribution as in Figures 2–4 during coronal mass ejection - sheath conditions.

firehose unstable conditions close to the magnetopause in the quasi-parallel magnetosheath (Figure 7c). Similar to Plaschke jets, the jet percentage close to the magnetopause seems to be increasing toward lower *A* (Figures 7c and 7d). However, the overall jet percentage is more evenly distributed for Archer jets compared to the Plaschke criterion.

4. Interpretation and Discussion

This work provides a general overview of the magnetosheath plasma behavior with respect to the most common proton instabilities and how it changes with location in the magnetosheath, conditions at the shock, and within magnetosheath jets. We herein discuss the physics of these observations (Section 4.1), the choice of instability thresholds (Section 4.2), and consider the context of magnetosheath jets (Section 4.3). Limitations in our measurements and methods may affect the sub-populations in the data (Section 4.4).

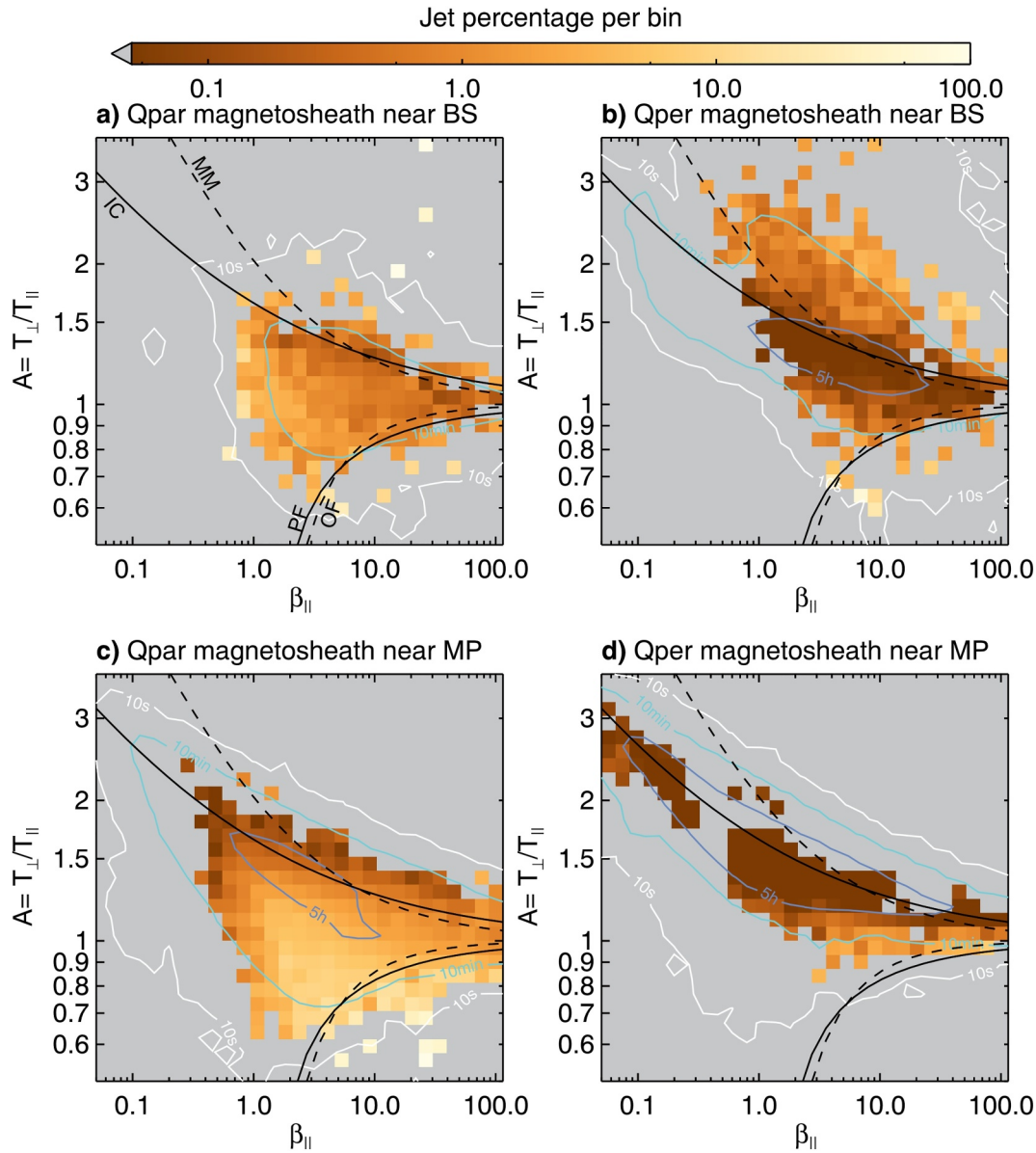

Figure 6. Dayside magnetosheath jet distribution in the A–$\beta_{\parallel}$ plane using Plaschke et al. (2013) criteria at the different magnetosheath locations defined in Figure 2. The total duration of magnetosheath measurements is given by the over-plotted contours.

4.1. Interpretation of the General Distributions

Figures 2a–2d shows the plasma behavior in quasi-perpendicular and quasi-parallel conditions, at the shock and close to the magnetopause. The following can be seen in the quasi-perpendicular region: The shock produces large perpendicular temperature anisotropies in its downstream region (Figure 2b), as expected from double-adiabatic invariant plasma theory and field compression effects (Crooker & Siscoe, 1977). While mostly bounded by the plasma instabilities, the plasma displays at $\beta_{\parallel} > 1$ a population in marginal instability with respect to the mirror mode instability. This population belongs to measurements close to the quasi-perpendicular shock crossing (specifically the gyrating, reflected ion population at the shock (Sckopke et al., 1983, 1990)) and is seemingly detached from the bulk population at marginal stability close to the ion cyclotron threshold. The plasma close to the shock retains some non-Maxwellian and agyrotropic behavior. Czaykowska et al. (1998, 2001) analyzed fluctuations downstream of quasi-perpendicular shocks, reporting the high anisotropic plasma population that

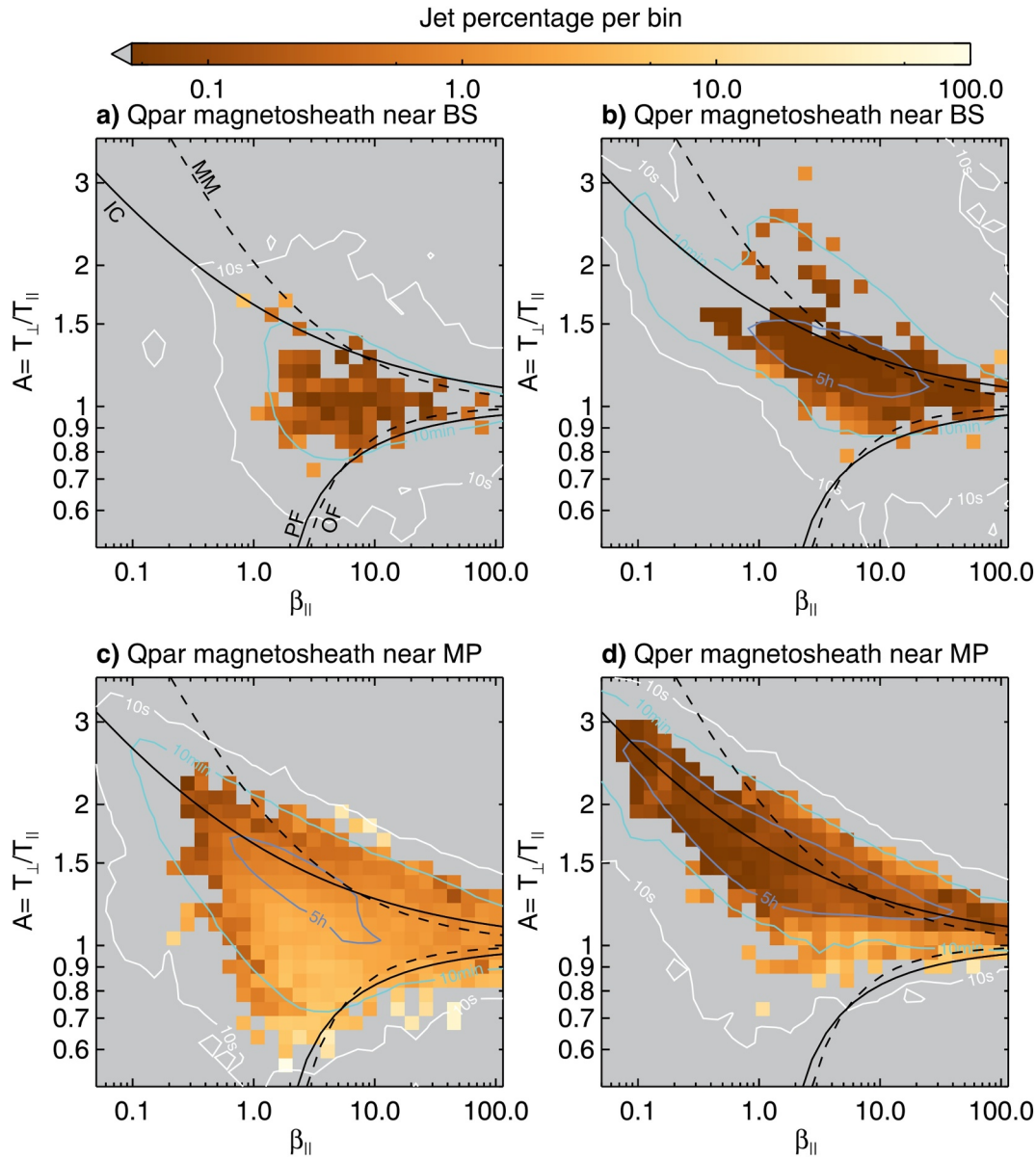

Figure 7. Dayside magnetosheath jet distribution in the A–$\beta_{\parallel}$ plane using Archer and Horbury (2013) criteria at the different magnetosheath locations defined in Figure 2. The total duration of magnetosheath measurements is given by the over-plotted contours.

fulfills the mirror mode criterion. Mirror mode waves themselves however are not always found even with the mirror mode criterion being fulfilled (Czaykowska et al., 2001). There are a few caveats to be considered when analyzing this population: Quickly changing magnetic field orientations can introduce uncertainty in the parallel and perpendicular temperature value, especially at spin-resolution. Effects of alpha particles, which can be substantial close to shock crossings (Preisser, Blanco-Cano, Trotta, et al., 2020), is not resolved in our case. Furthermore, due to the spacecraft orbit being statistically low (see discussions by Vuorinen, LaMoury, et al., 2023), shock crossings might be biased toward high Mach number and correlated high β values, possibly skewing the values toward the mirror mode regime. Therefore, a more detailed and careful analysis is required on this population beyond the scope of the present work. By the time the plasma reaches the magnetopause (Figure 2d), this population high beyond the defined mirror mode threshold greatly reduces. This apparent relaxation from shock to magnetopause is consistent with mirror modes being generated and consuming the free energy in the plasma (Génot et al., 2011; Soucek et al., 2008). Close to the magnetopause, the overall distribution

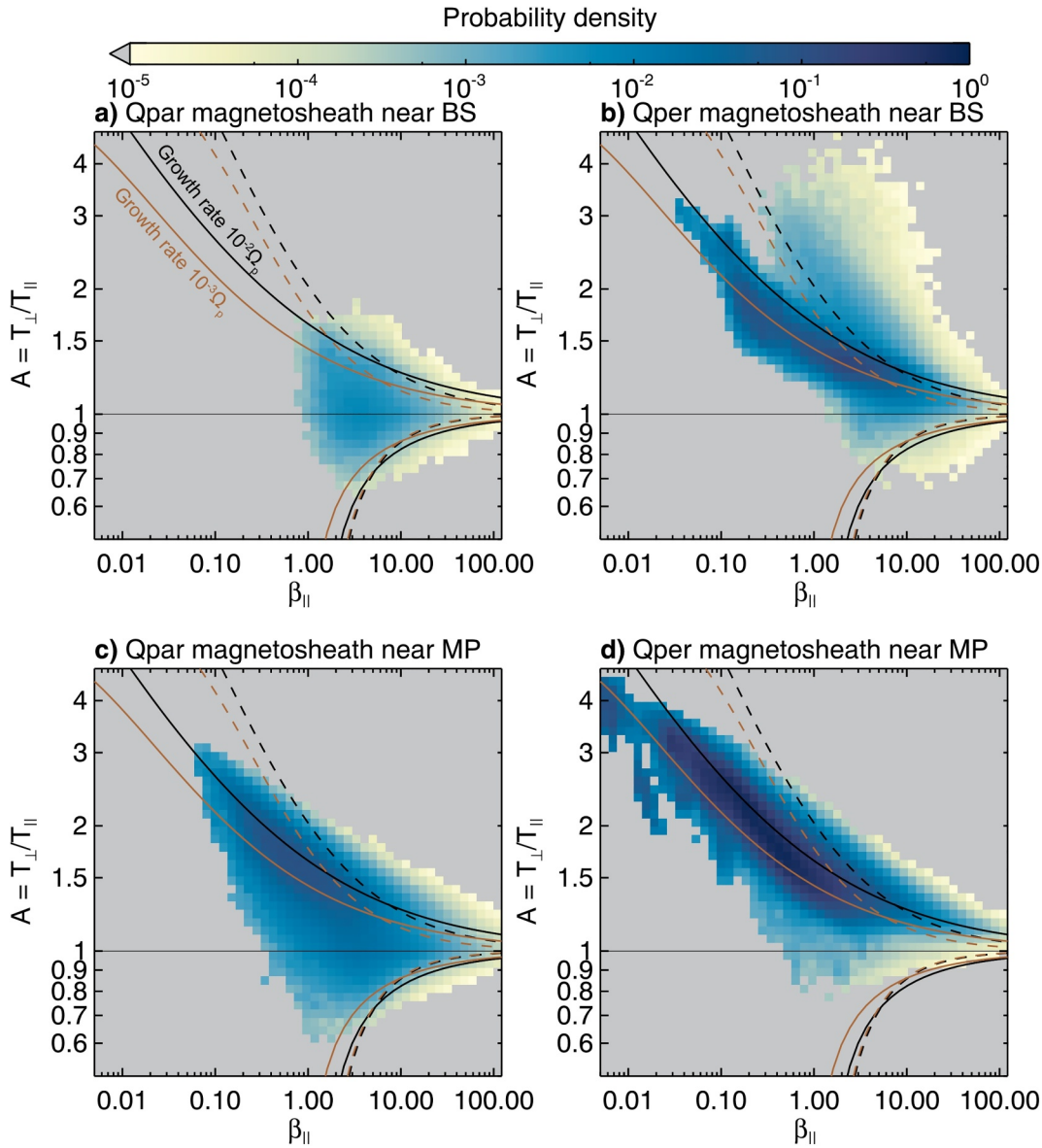

Figure 8. Statistical plasma distributions of A versus $\beta_{||}$ in the four different magnetosheath regions showing the results from Figure 2. We compare 10^{-2} Ω_p (black lines) and 10^{-3} Ω_p (brown lines) growth rates.

is skewed toward low plasma $\beta_{||}$/high A regions. This behavior is consistent with field compression (conservation of the adiabatic invariants close to the magnetopause resulting in increased A) and large magnetic field intensities at the magnetopause (increase in magnetic pressure and decrease in $\beta_{||}$) (Crooker et al., 1979; Génot et al., 2011; Schwartz et al., 1996).

In comparison, the quasi-parallel conditions downstream of the shock is expected to show a primarily isotropic ion plasma temperature and consequently plasma conditions that are less prone to temperature-driven ion plasma instabilities. In Figure 2a, the plasma appears to be primarily in stable conditions with respect to all instabilities, peaking distribution around $A \sim 1$, and $\beta_{||} \sim 4$. Close to the magnetopause, the distribution broadens significantly with a population marginally unstable to the ion cyclotron and mirror mode instabilities. Similar to the quasi-perpendicular case, this behavior is consistent with field compression due to the presence of the magnetopause in its vicinity. Strong compressive fluctuations, which are expected in the quasi-parallel magnetosheath,

could play an additional role in systematically scattering the distribution within the A–$\beta_{\parallel}$ plane and causing isotropization (Verscharen et al., 2016).

4.2. Choice of Plasma Stability Thresholds

The choice of threshold provides a general assessment tool of the global instability conditions. Our quantification of measurements within each defined stability regime gives an overview, while individual case analysis would require wave mode analysis to check whether the instability was triggered and in-depth polarization analysis. We employ instability thresholds using a growth rate of 10^{-2} Ω_p. This is based on thresholds fitted to MMS magnetosheath measurements in Maruca et al. (2018) (using six intervals of strong turbulence activity). Growth rates between $10^{-2.25}$ and $10^{-1.5}$ Ω_p matched their distribution best. Recent works by Lewis et al. (2024) and Jiang et al. (2025) employed a growth rate of 10^{-2} Ω_p, with the latter one exploring the resulting change when transitioning to a lower growth rate of 10^{-3} Ω_p as well. Figure 8 shows the results from Figure 2 comparing 10^{-2} Ω_p and 10^{-3} Ω_p growth rates using the parameters by Verscharen et al. (2016). Substantial differences in the total number of points within the stable and unstable regimes arise, especially in the quasi-perpendicular regime close to the magnetopause (Figure 8d). Here, we see a change from 66% toward 16% of plasma in stable regime when transitioning from the high to the low growth rate. The fact that the bulk of the measurements are situated along the instability threshold following expected growth rates can be indicative: The plasma seemingly accumulates there in parameter space, possibly due to a balance of anisotropy being introduced and the instability acting on the plasma, putting it back into marginal stability. There is little change to the number of measurements prone to parallel and oblique firehose stability, as we see differences at roughly 1% or less when transitioning from low to high growth rates.

4.3. Plasma Stability in Magnetosheath Jets

Magnetosheath jets show primarily stable conditions (in total 89% for Plaschke criteria jets and 84% for Archer criteria jets), which matches with main formation mechanisms currently discussed in the community (Krämer et al., 2025; Plaschke et al., 2018). Hietala et al. (2009) proposed that jets form due to the solar wind being less decelerated and thermalized at rippled bow shock patches, thus, causing plasma flows less shocked than the surrounding plasma. Raptis, Karlsson, Vaivads, Pollock, et al. (2022) showed a case study of jet formation due to solar wind being trapped between patches of the constantly reforming bow shock. Raptis, Karlsson, Vaivads, Lindberg, et al. (2022) showed one case of a jet consisting of two different plasma populations: the thermalized magnetosheath plasma and a colder, solar-wind-like plasma population. Solar wind plasma is primarily in stable conditions (e.g., Hellinger et al., 2006). Thus, the aforementioned jet studies could point toward the expectation of jets showing stable plasma as well. Similarly, Blanco-Cano et al. (2020) analyzed jets with $A \sim 1$, noting that the isotropy occurs due to two populations co-existing in the velocity distribution function inside the jets. A detailed analysis akin to the methods used in Raptis, Karlsson, Vaivads, Lindberg, et al. (2022) is recommended to future studies on the behavior of overlapping plasma populations in jets. Whether this behavior within jets holds in general or is restricted to certain events, and what effect two jet plasma populations could have on the analysis of plasma instabilities in terms of linear perturbation theory remain to be analyzed in the future. While most jets appear to be more isotropic than the surrounding magnetosheath (Plaschke et al., 2013), individual case studies however have shown a variety of A values in jets: Blanco-Cano et al. (2023) analyzed a jet with $A < 1$, resembling a flux transfer event, and jets with $A > 1$ in mirror mode unstable conditions, possibly connected to reconnection. Both Blanco-Cano et al. (2020) and Blanco-Cano et al. (2023) showed that A can fluctuate within jets.

The excess of jets identified by the Plaschke criterion near the quasi-perpendicular shock transition layer requires further investigation, as these match the so-called gyro-bunched jet events discussed in Vuorinen, LaMoury, et al. (2023). Recent results by Osmane and Raptis (2024) suggest that jets may form via plasma instabilities, particularly the firehose instability. Using MMS burst data, they report that 11% of all jet-associated measurements near the quasi-parallel bow shock are firehose unstable, implying a connection between jets and the instability. While our data is limited to 3 s resolution, we indeed find plasma within magnetosheath jets to be 2–8 times more likely to be unstable to firehose instabilities compared to the average magnetosheath.

Plaschke et al. (2018) showed that the Plaschke et al. (2013) jet criterion is more restrictive than the Archer and Horbury (2013) criterion. The latter may detect instances of the upper end of the dynamic pressure as jet events,

which would explain why the jet percentage is more evenly distributed (Figure 7). The Archer criterion may also classify other structures (such as large mirror modes, which manifest as anti-phase magnetic field and density variations) as jets. Recently, Jiang et al. (2025) showed one instance of mirror mode instabilities with strong dynamic pressure enhancements. Those could qualify as jets under the Archer criterion. This interpretation could explain the increase in jet percentage (Figures 7c and 7d) in mirror-mode unstable conditions.

4.4. Limitations

Our differentiation into quasi-parallel and quasi-perpendicular magnetosheath as described in Appendix B uses both ion energy flux and θ_{Bn} restrictions to ensure reliable classifications. The different distributions (Figures 2a and 2b) prove the detection of different plasma regions, which follow well the qualitative expectation of higher A at the quasi-perpendicular shock compared to the values found at the quasi-parallel shock (Karlsson et al., 2021; Svenningsson et al., 2025). The differentiation partly relies on the OMNI-derived magnetic field propagated values from L1-located solar wind monitors to the bow shock nose. We avoid the intermediate range of angles corresponding to oblique shocks ($30° < \theta_{Bn} < 60°$). The impact of high intrinsic ion energy fluxes during HSSs are considered to improve the classification (Koller et al., 2024). We exclude the intermediate range of the relative magnetosheath spacecraft position ($0.33 < F < 0.66$) in order to compare the different populations close to the bow shock and close to the magnetopause. The fact that the excess population of high $A > 2.5$ and high $\beta_{\parallel} > 1$ plasma associated with quasi-perpendicular bow shock transition layer in Figure 2b completely vanishes close to the magnetopause (Figure 2d) is a good indicator of the validity of our approach.

The analysis on the effect of heavy ions (such as alpha particles), which are known to alter instability conditions in the plasma, is left to a future study. Solar wind alpha particles have relatively large A (e.g., Li et al., 2023; Preisser, Blanco-Cano, Trotta, et al., 2020), which provide an extra source of free energy for instability growth (Maruca et al., 2012; Price et al., 1986). CMEs show higher alpha/proton ratios compared to other structures (around 5%, Xu & Borovsky, 2015; Y. Zhang et al., 2022), possibly increasing the temperature anisotropy further during these events. Results in the A–$\beta_{\parallel}$ plane can change on different temporal resolutions (Opie et al., 2022). With a spin-limited resolution of 3 s in the present THEMIS data sets used here, effects on shorter timescales, above the local ion gyrofrequency, will be lost, although magnetosheath ULF wave mode structures at ion scales (such as mirror modes) usually appear on typical timescales of 1–20 s in the Earth's magnetosheath (Génot et al., 2011; Soucek et al., 2008).

5. Conclusions

In this work we provide comprehensive general plasma statistics of the dayside magnetosheath with respect to the most common kinetic plasma instabilities (mirror mode, ion cyclotron, parallel, and oblique firehose). We show with THEMIS data how the overall ion distributions, assumed to be protons, vary between quasi-parallel and quasi-perpendicular magnetosheath, both close to the bow shock and magnetopause, with respect to these instabilities. We investigate the stability in the $A = T_{\perp}/T_{\parallel}$–$\beta_{\parallel}$ plane. The resulting distributions are influenced by upstream solar wind structures, such as magnetic ejecta of CMEs (CME-MEs), CME-driven shock and sheaths (CME-SH), and HSSs. As an immediate application of the statistical analysis, we investigate the plasma inside magnetosheath jets with respect to the main plasma instabilities.

The main results are as follows:

- Quasi-parallel versus quasi-perpendicular shock conditions: The plasma is generally more stable with respect to the main plasma instabilities in the quasi-parallel magnetosheath and more isotropic than in the quasi-perpendicular one, in line with theoretical expectations.
- Variation with respect to distance in the magnetosheath: The quasi-parallel magnetosheath exhibits mostly marginally stable conditions near the shock with growing anisotropy closer to the magnetopause. This demonstrates that the source of the free energy available for the waves is closer to the magnetopause. The quasi-perpendicular magnetosheath contains on average a large A immediately downstream of the shock, which continues to grow toward the magnetopause. The population above the mirror-mode threshold at very large A near the shock vanishes the closer to the magnetopause and is associated with the shock transition layer.

- Influence of solar wind structures: Close to the shock, the magnetosheath undergoing HSSs usually has plasma $\beta_{\parallel} > 0.5$, regardless of shock geometry. The magnetosheath under CME-magnetic ejecta and CME-sheath conditions, while showing increased A, appear mostly marginally stable near the shock, regardless of shock geometry. CME-magnetic ejecta are the cause for the most extreme low $\beta_{\parallel}$–high A values in the magnetosheath due to strong magnetic fields and low Mach numbers. HSSs cause in general more instances of plasma unstable to the mirror-mode and oblique firehose compared to measurements associated with CMEs.
- Inside magnetosheath jets: the Plaschke et al. (2013) criteria jets are primarily stable with respect to the main instabilities everywhere in the magnetosheath, except for a sub-population close to the quasi-perpendicular shock. Jets are more prominently seen in the quasi-parallel sheath. The Archer and Horbury (2013) criteria jets follow the same trend, however with the measurements being more evenly distributed across the background distribution. This could be a result of the detection criterion being not as strict, which may capture other transient structures due to the magnetosheath's intrinsic fluctuations than jets proper. Close to the magnetopause, Archer-criterion jets appear more prominently at the upper limit of the distribution in the mirror-mode unstable region compared to Plaschke-criterion jets. This indicates that the criterion might pick up on mirror modes and classify them as jets. Jets detected from both criteria are more common in the very few measurements below the firehose instabilities compared to the total distribution we see in the magnetosheath.

Connecting the analysis with upstream conditions and incoming structures provides context for the range of possible magnetosheath plasma parameters and instabilities. Every structure that ultimately impacts Earth's magnetosphere—and potentially human infrastructure—is modified by the shock and magnetosheath. Understanding how upstream plasma is shaped by these regions is therefore crucial. Jets are one pathway for energy transfer from the shock to the magnetosphere. Our work helps clarify their connection to plasma instabilities, pointing to the existence of distinct jet subpopulations.

Appendix A: Relative Magnetosheath Distance and θ_{Bn}

We use magnetopause and bow shock models to derive the relative distance in the magnetosheath and the estimated IMF angle at the shock θ_{Bn} sunward of the spacecraft's position. We follow the approach of Svenningsson et al. (2025): We use the Shue et al. (1998) model for the magnetopause. The radial distance of the magnetopause along a certain angle ϕ to the sun-earth line is defined as

$$r_{MP} = r_{0,MP}\left(\frac{2}{1+\cos\phi}\right)^{\alpha}, \tag{A1}$$

where $r_{0,MP}$ denotes the standoff distance, and α the level of tail flaring. $r_{0,MP}$ and α are empirical relations and are given by Equations 10 and 11 in Shue et al. (1998), respectively. Both depend on the IMF z component in GSM coordinates $b_{z,GSM}$ and the solar wind dynamic pressure $p_{dyn,SW}$, for which we use the 1 min resolution values by OMNI. We follow Merka et al. (2003) to derive the bow shock distance: the shape of the bow shock is described by a simple parabolic equation $X = a_s - b_s\left(Y^2 + Z^2\right)$. The bow shock nose standoff distance a_s is defined in Equation 23 of Farris and Russell (1994) and depends on $r_{0,MP}$, α, and the solar wind fast mode Mach number. The bow shock flaring parameter b_s is given by Equation 11 in Fairfield et al. (2001) and depends on a_s, $p_{dyn,SW}$, and the Alfvén Mach number M_A. We again use 1 min resolution OMNI values as input parameter.

The distance of the bow shock using ϕ corresponding to the spacecraft position is calculated. The final relative spacecraft position is derived following Archer and Horbury (2013):

$$F = \frac{r - r_{MP}}{r_{BS} - r_{MP}}. \tag{A2}$$

r_{BS} denotes the radial distance of the bow shock and r_{MP} the radial distance of the magnetopause, both along the Earth-spacecraft line, with $F = 0$ ($F = 1$) meaning that the spacecraft is at the magnetopause (bow shock). Each model can have significant uncertainties on the bow shock and magnetopause distances, and consequently on the relative spacecraft position. Therefore, this work only utilizes restricted regions close to the magnetopause ($F < 0.33$) and the bow shock ($F > 0.66$).

Using the described parabolic equation for the bow shock above, we calculate the angle at the bow shock directly sunward (GSE-X) of the spacecraft's position. The shock normal vector is derived at the local bow shock surface position. θ_{Bn} is then calculated as the angle between the shock normal and the OMNI IMF.

Appendix B: Definition of Quasi-Parallel and Quasi-Perpendicular Sheath in THEMIS Data

We follow the approach by Karlsson et al. (2021) to differentiate the magnetosheath into quasi-parallel and quasi-perpendicular geometries. We sum up the highest 3 energy bins of the THEMIS ESA instrument ($F_{high,3}$, roughly covering the ranges of 11–25 keV) to find highly energized ion populations, indicative of presence of the foreshock. The resulting distribution is divided into a high- and low-energy regime, which corresponds to quasi-parallel and quasi-perpendicular magnetosheath, respectively. As recently shown by Koller et al. (2024), fast solar wind (which generally aligns with HSSs) can cause misclassification. To account for this, the thresholds for $F_{high,3}$ to differentiate quasi-parallel from quasi-perpendicular sheaths are set as follows: based on Figure 5 in Koller et al. (2024), we use a threshold of 0.2×10^9 eV cm^{-2} s^{-1} sr^{-1} for quiet solar wind, CME-MEs, and CME-SH, and 1.6×10^9 eV cm^{-2} s^{-1} sr^{-1} for HSSs.

To increase the robustness of the differentiation, we restrict θ_{Bn} ($\theta_{Bn} > 60°$ for quasi-perpendicular, $\theta_{Bn} < 30°$ for quasi-parallel magnetosheath). This magnetosheath classification omits intermediate θ_{Bn} angles, minimizing cross-contamination of wrongly classified intervals. Figure B1 showcases a time interval where THEMIS A switches between quasi-parallel and quasi-perpendicular magnetosheath, visible in the high energy bins of the ion energy spectrum. The categorization happens only when both criteria defined above are met. This time range uses the threshold for slow solar wind.

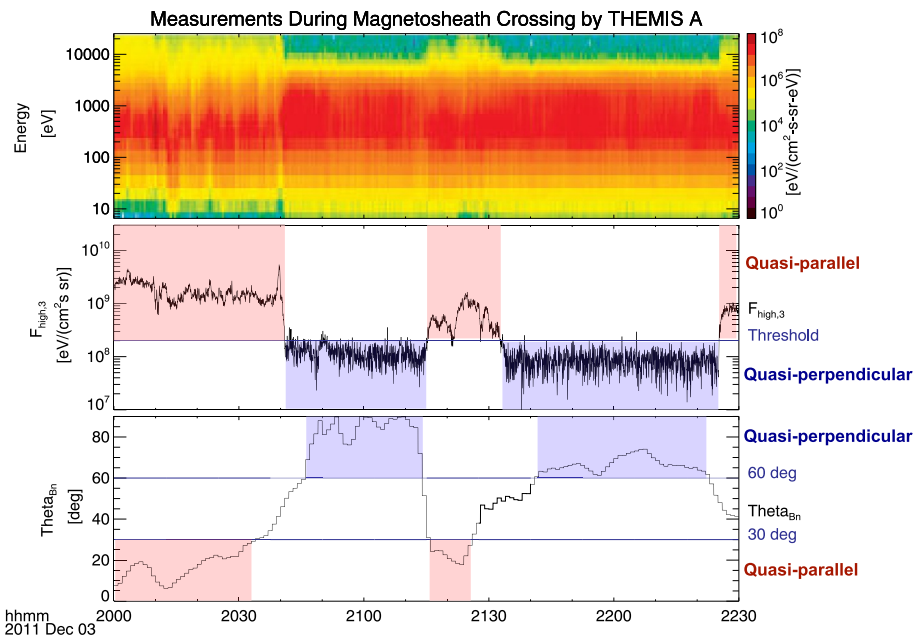

Figure B1. Example measurements of THEMIS A for differentiating quasi-parallel and quasi-perpendicular. From top to bottom: ion energy spectrum, $F_{high,3}$, and θ_{Bn}. The defined thresholds are given. A time interval is defined as quasi-parallel or quasi-perpendicular only when both conditions based on ion energy and shock angle are met.

Data Availability Statement

We thank C. W. Carlson and J. P. McFadden for use of ESA data. We acknowledge the use of NASA/GSFC's Space Physics Data Facility's OMNI data and web services (https://omniweb.gsfc.nasa.gov/html/omni_min_data.html). THEMIS and OMNI data were accessed using the SPEDAS software (Angelopoulos et al., 2019). The list of magnetosheath subintervals (2008–2023) of THEMIS spacecraft and detected jets therein based on the Plaschke et al. (2013), Archer and Horbury (2013), and Koller et al. (2022) criteria as well as the list of solar wind stream interaction regions and high-speed-streams in OMNI (1995–2023) is provided in Koller (2025).

Acknowledgments
F.K., M.T., L.P., O.R., and F.P. gratefully acknowledge the Austrian Science Fund (FWF): P 33285-N for supporting this project. The authors acknowledge the financial support by the University of Graz. F.K. and C.H.K.C. are supported by STFC Consolidated Grant ST/X000974/1. P.A.S. and C.H.K.C. are supported by UKRI Future Leaders Fellowship MR/W007657/1. We acknowledge NASA contract NAS5-02099 and V. Angelopoulos for use of data from the THEMIS Mission. C.S.W. is supported by the Austrian Science Fund (FWF) 10.55776/P35954. Z.V. and O.W.R. were supported by the Austrian Science Fund (FWF) 10.55776/P37265. Z.V. was also supported by the Austrian Science Fund (FWF) 10.55776/PAT9232923. I.S. is supported by the Swedish Research Council Grant 2016-0550, the Swedish National Space Agency Grant 158/16, and the Knut and Alice Wallenberg foundation (Dnr. 2022.0087). Specifically we thank K.H. Glassmeier, H.U. Auster and W. Baumjohann for the use of FGM data provided under the lead of the Technical University of Braunschweig and with financial support through the German Ministry for Economy and Technology and the German Center for Aviation and Space (DLR) under contract 50 OC 0302. A.P. and F.P. acknowledge the support by the Deutsches Zentrum für Luft-und Raumfahrt under contract 50 OC 2201.

References

Ala-Lahti, M. M., Kilpua, E. K. J., Dimmock, A. P., Osmane, A., Pulkkinen, T., & Souček, J. (2018). Statistical analysis of mirror mode waves in sheath regions driven by interplanetary coronal mass ejection. *Annales Geophysicae*, *36*(3), 793–808. https://doi.org/10.5194/angeo-36-793-2018

Alterman, B. L., & Kasper, J. C. (2019). Helium variation across two solar cycles reveals a speed-dependent phase lag. *The Astrophysical Journal Letters*, *879*(1), L6. https://doi.org/10.3847/2041-8213/ab2391

Anderson, B. J., & Fuselier, S. A. (1993). Magnetic pulsations from 0.1 to 4.0 Hz and associated plasma properties in the Earth's subsolar magnetosheath and plasma depletion layer. *Journal of Geophysical Research*, *98*(A2), 1461–1480. https://doi.org/10.1029/92JA02197

Angelopoulos, V. (2008). The THEMIS mission. *Space Science Reviews*, *141*(1–4), 5–34. https://doi.org/10.1007/s11214-008-9336-1

Angelopoulos, V., Cruce, P., Drozdov, A., Grimes, E. W., Hatzigeorgiu, N., King, D. A., et al. (2019). The space physics environment data analysis system (SPEDAS). *Space Science Reviews*, *215*(1). https://doi.org/10.1007/s11214-018-0576-4

Archer, M. O., & Horbury, T. S. (2013). Magnetosheath dynamic pressure enhancements: Occurrence and typical properties. *Annales Geophysicae*, *31*(2), 319–331. https://doi.org/10.5194/angeo-31-319-2013

Artemyev, A. V., Shi, C., Lin, Y., Nishimura, Y., Gonzalez, C., Verniero, J., et al. (2022). Ion kinetics of plasma flows: Earth's magnetosheath versus solar wind. *The Astrophysical Journal*, *939*(2), 85. https://doi.org/10.3847/1538-4357/ac96e4

Auster, H. U., Glassmeier, K. H., Magnes, W., Aydogar, O., Baumjohann, W., Constantinescu, D., et al. (2008). The THEMIS fluxgate magnetometer. *Space Science Reviews*, *141*(1–4), 235–264. https://doi.org/10.1007/s11214-008-9365-9

Balogh, A., & Treumann, R. A. (2013). Physics of collisionless shocks (Vol. *12*). https://doi.org/10.1007/978-1-4614-6099-2

Bandyopadhyay, R., Qudsi, R. A., Gary, S. P., Matthaeus, W. H., Parashar, T. N., Maruca, B. A., et al. (2022). Interplay of turbulence and proton-microinstability growth in space plasmas. *Physics of Plasmas*, *29*(10), 102107. https://doi.org/10.1063/5.0098625

Blanco-Cano, X., Preisser, L., Kajdič, P., & Rojas-Castillo, D. (2020). Magnetosheath microstructure: Mirror mode waves and jets during southward IP magnetic field. *Journal of Geophysical Research: Space Physics*, *125*(9), e27940. https://doi.org/10.1029/2020JA027940

Blanco-Cano, X., Rojas-Castillo, D., Kajdič, P., & Preisser, L. (2023). Jets and mirror mode waves in earth's magnetosheath. *Journal of Geophysical Research: Space Physics*, *128*(7), e2022JA031221. https://doi.org/10.1029/2022JA031221

Burch, J. L., Moore, T. E., Torbert, R. B., & Giles, B. L. (2016). Magnetospheric Multiscale overview and science objectives. *Space Science Reviews*, *199*(1–4), 5–21. https://doi.org/10.1007/s11214-015-0164-9

Chao, J. K., Zhang, X. X., & Song, P. (1995). Derivation of temperature anisotropy from shock jump relations: Theory and observations. *Geophysical Research Letters*, *22*(17), 2409–2412. https://doi.org/10.1029/95GL02187

Crooker, N. U., Eastman, T. E., & Stiles, G. S. (1979). Observations of plasma depletion in the magnetosheath at the dayside magnetopause. *Journal of Geophysical Research*, *84*(A3), 869–874. https://doi.org/10.1029/JA084iA03p00869

Crooker, N. U., & Siscoe, G. L. (1977). A mechanism for pressure anisotropy and mirror instability in the dayside magnetosheath. *Journal of Geophysical Research*, *82*(1), 185–186. https://doi.org/10.1029/JA082i001p00185

Czaykowska, A., Bauer, T. M., Treumann, R. A., & Baumjohann, W. (1998). Mirror waves downstream of the quasi-perpendicular bow shock. *Journal of Geophysical Research*, *103*(A3), 4747–4752. https://doi.org/10.1029/97JA03245

Czaykowska, A., Bauer, T. M., Treumann, R. A., & Baumjohann, W. (2001). Magnetic field fluctuations across the Earth's bow shock. *Annales Geophysicae*, *19*(3), 275–287. https://doi.org/10.5194/angeo-19-275-2001

DeWeese, H., Maruca, B. A., Qudsi, R. A., Chasapis, A., Pultrone, M., Johnson, E., et al. (2022). Alpha particle temperature anisotropy in Earth's magnetosheath. *The Astrophysical Journal*, *941*(1), 12. https://doi.org/10.3847/1538-4357/ac9791

Dimmock, A. P., & Nykyri, K. (2013). The statistical mapping of magnetosheath plasma properties based on themis measurements in the magnetosheath interplanetary medium reference frame. *Journal of Geophysical Research: Space Physics*, *118*(8), 4963–4976. https://doi.org/10.1002/jgra.50465

Dimmock, A. P., Osmane, A., Pulkkinen, T. I., & Nykyri, K. (2015). A statistical study of the dawn-dusk asymmetry of ion temperature anisotropy and mirror mode occurrence in the terrestrial dayside magnetosheath using THEMIS data. *Journal of Geophysical Research: Space Physics*, *120*(7), 5489–5503. https://doi.org/10.1002/2015JA021192

Eastwood, J. P., Lucek, E. A., Mazelle, C., Meziane, K., Narita, Y., Pickett, J., & Treumann, R. A. (2005). The foreshock. *Space Science Reviews*, *118*(1–4), 41–94. https://doi.org/10.1007/s11214-005-3824-3

Escoubet, C. P., Schmidt, R., & Goldstein, M. L. (1997). Cluster - Science and mission overview. *Space Science Reviews*, *79*(1/2), 11–32. https://doi.org/10.1023/A:1004923124586

Fairfield, D. H., Iver, H. C., Desch, M. D., Szabo, A., Lazarus, A. J., & Aellig, M. R. (2001). The location of low mach number bow shocks at earth. *Journal of Geophysical Research*, *106*(A11), 25361–25376. https://doi.org/10.1029/2000JA000252

Farris, M. H., & Russell, C. T. (1994). Determining the standoff distance of the bow shock: Mach number dependence and use of models. *Journal of Geophysical Research*, *99*(A9), 17681–17689. https://doi.org/10.1029/94JA01020

Gary, S. P. (1992). The mirror and ion cyclotron anisotropy instabilities. *Journal of Geophysical Research*, *97*(A6), 8519–8529. https://doi.org/10.1029/92JA00299

Gary, S. P., Anderson, B. J., Denton, R. E., Fuselier, S. A., McKean, M. E., & Winske, D. (1993). Ion anisotropies in the magnetosheath. *Geophysical Research Letters*, *20*(17), 1767–1770. https://doi.org/10.1029/93GL01700

Génot, V., Broussillou, L., Budnik, E., Hellinger, P., Trávníček, P. M., Lucek, E., & Dandouras, I. (2011). Timing mirror structures observed by Cluster with a magnetosheath flow model. *Annals of Geophysics*, *29*(10), 1849–1860. https://doi.org/10.5194/angeo-29-1849-2011

Goncharov, O., Gunell, H., Hamrin, M., & Chong, S. (2020). Evolution of high-speed jets and plasmoids downstream of the quasi-perpendicular bow shock. *Journal of Geophysical Research: Space Physics*, *125*(6), e2019JA027667. https://doi.org/10.1029/2019JA027667

Gurchumelia, A., Sorriso-Valvo, L., Burgess, D., Yordanova, E., Elbakidze, K., Kharshiladze, O., & Kvaratskhelia, D. (2022). Comparing quasi-parallel and quasi-perpendicular configuration in the terrestrial magnetosheath: Multifractal analysis. *Frontiers in Physics*, *10*, 903632. https://doi.org/10.3389/fphy.2022.903632

Hellinger, P., Matteini, L., Landi, S., Franci, L., Verdini, A., & Papini, E. (2019). Turbulence versus fire-hose instabilities: 3D hybrid expanding box simulations. *The Astrophysical Journal*, *883*(2), 178. https://doi.org/10.3847/1538-4357/ab3e01

Hellinger, P., Trávníček, P., Kasper, J. C., & Lazarus, A. J. (2006). Solar wind proton temperature anisotropy: Linear theory and WIND/SWE observations. *Geophysical Research Letters*, *33*(9), 2006GL025925. https://doi.org/10.1029/2006GL025925

Hietala, H., Laitinen, T. V., Andréeová, K., Vainio, R., Vaivads, A., Palmroth, M., et al. (2009). Supermagnetosonic jets behind a collisionless quasiparallel shock. *Physical Review Letters*, *103*(24), 20–23. https://doi.org/10.1103/PhysRevLett.103.245001

Hietala, H., Partamies, N., Laitinen, T. V., Clausen, L. B. N., Facskó, G., Vaivads, A., et al. (2012). Supermagnetosonic subsolar magnetosheath jets and their effects: From the solar wind to the ionospheric convection. *Annales Geophysicae*, *30*(1), 33–48. https://doi.org/10.5194/angeo-30-33-2012

Hietala, H., Trotta, D., Fedeli, A., Wilson, L. B., Vuorinen, L., & Coburn, J. T. (2024). Candidates for downstream jets at interplanetary shocks. *Monthly Notices of the Royal Astronomical Society*, *531*(2), 2415–2421. https://doi.org/10.1093/mnras/stae1294

Jiang, W., Li, H., Yang, Z., Verscharen, D., & Wang, C. (2025). Spatial dependence of ion-kinetic instabilities in the earth's magnetosheath: Mms observations. *Journal of Geophysical Research: Space Physics*, *130*(3), e2024JA033463. https://doi.org/10.1029/2024JA033463

Kajdič, P., Raptis, S., Blanco-Cano, X., & Karlsson, T. (2021). Causes of jets in the quasi-perpendicular magnetosheath. *Geophysical Research Letters*, *48*(13), e93173. https://doi.org/10.1029/2021GL093173

Karlsson, T., Raptis, S., Trollvik, H., & Nilsson, H. (2021). Classifying the magnetosheath behind the quasi-parallel and quasi-perpendicular bow shock by local measurements. *Journal of Geophysical Research: Space Physics*, *126*(9), e2021JA029269. https://doi.org/10.1029/2021JA029269

Kasper, J. C., Stevens, M. L., Lazarus, A. J., Steinberg, J. T., & Ogilvie, K. W. (2007). Solar wind helium abundance as a function of speed and heliographic latitude: Variation through a solar cycle. *The Astrophysical Journal*, *660*(1), 901–910. https://doi.org/10.1086/510842

King, J. H., & Papitashvili, N. E. (2005). Solar wind spatial scales in and comparisons of hourly Wind and ACE plasma and magnetic field data. *Journal of Geophysical Research: Space Physics*, *110*(A2), A02104. https://doi.org/10.1029/2004JA010649

Koller, F. (2025). *Themis dayside magnetosheath intervals and detected jets 2008 - 2023; sir and hss event lists 1995-2023*. Zenodo. Retrieved from https://zenodo.org/records/13843752

Koller, F., Plaschke, F., Temmer, M., Preisser, L., Roberts, O. W., & Vörös, Z. (2023). Magnetosheath jet formation influenced by parameters in solar wind structures. *Journal of Geophysical Research: Space Physics*, *128*(4), e2023JA031339. https://doi.org/10.1029/2023JA031339

Koller, F., Raptis, S., Temmer, M., & Karlsson, T. (2024). The effect of fast solar wind on ion distribution downstream of earth's bow shock. *The Astrophysical Journal Letters*, *964*(1), L5. https://doi.org/10.3847/2041-8213/ad2ddf

Koller, F., Temmer, M., Preisser, L., Plaschke, F., Geyer, P., Jian, L. K., et al. (2022). Magnetosheath jet occurrence rate in relation to CMEs and SIRs. *Journal of Geophysical Research: Space Physics*, *127*(4), e2021JA030124. https://doi.org/10.1029/2021JA030124

Krämer, E., Koller, F., Suni, J., LaMoury, A. T., Pöppelwerth, A., Glebe, G., et al. (2025). Jets downstream of collisionless shocks: Recent discoveries and challenges. *Space Science Reviews*, *221*(1), 4. https://doi.org/10.1007/s11214-024-01129-3

LaMoury, A. T., Hietala, H., Plaschke, F., Vuorinen, L., & Eastwood, J. P. (2021). Solar wind control of magnetosheath jet formation and propagation to the magnetopause. *Journal of Geophysical Research: Space Physics*, *126*(9), e2021JA029592. https://doi.org/10.1029/2021JA029592

Lewis, H. C., Stawarz, J. E., Matteini, L., Franci, L., Klein, K. G., Wicks, R. T., et al. (2024). Turbulent energy conversion associated with kinetic microinstabilities in earth's magnetosheath. *Geophysical Research Letters*, *51*(24), e2024GL112038. https://doi.org/10.1029/2024GL112038

Li, Q. H., Xiang, L., Wu, D. J., Chen, L., Zhao, G. Q., Zhao, A. K., et al. (2023). Distribution of alpha temperature anisotropy in the slow and fast solar wind: WIND observations and Vlasov theory. *A&A*, *676*, A137. https://doi.org/10.1051/0004-6361/202346815

Liu, Y., Richardson, J. D., Belcher, J. W., Kasper, J. C., & Skoug, R. M. (2006). Plasma depletion and mirror waves ahead of interplanetary coronal mass ejections. *Journal of Geophysical Research: Space Physics*, *111*(A9). https://doi.org/10.1029/2006JA011723

Maruca, B. A., Chasapis, A., Gary, S. P., Bandyopadhyay, R., Chhiber, R., Parashar, T. N., et al. (2018). *MMS* observations of beta-dependent constraints on ion temperature anisotropy in Earth's magnetosheath. *The Astrophysical Journal*, *866*(1), 25. https://doi.org/10.3847/1538-4357/aaddfb

Maruca, B. A., Kasper, J. C., & Gary, S. P. (2012). Instability-driven limits on helium temperature anisotropy in the solar wind: Observations and linear Vlasov analysis. *The Astrophysical Journal*, *748*(2), 137. https://doi.org/10.1088/0004-637X/748/2/137

Matteini, L., Hellinger, P., Landi, S., Trávníček, P. M., & Velli, M. (2012). Ion kinetics in the solar wind: Coupling global expansion to local microphysics. *Space Science Reviews*, *172*(1–4), 373–396. https://doi.org/10.1007/s11214-011-9774-z

McFadden, J. P., Carlson, C. W., Larson, D., Ludlam, M., Abiad, R., Elliott, B., et al. (2008). The THEMIS ESA plasma instrument and in-flight calibration. *Space Science Reviews*, *141*(1–4), 277–302. https://doi.org/10.1007/s11214-008-9440-2

Merka, J., Szabo, A., Narock, T. W., King, J. H., Paularena, K. I., & Richardson, J. D. (2003). A comparison of imp 8 observed bow shock positions with model predictions. *Journal of Geophysical Research*, *108*(A2). https://doi.org/10.1029/2002JA009384

Opie, S., Verscharen, D., Chen, C. H. K., Owen, C. J., & Isenberg, P. A. (2022). Conditions for proton temperature anisotropy to drive instabilities in the solar wind. *The Astrophysical Journal*, *941*(2), 176. https://doi.org/10.3847/1538-4357/ac982f

Osmane, A., & Raptis, S. (2024). On the formation of super-Alfvénic flows downstream of collisionless shocks. *The Astrophysical Journal*, *976*(1), 104. https://doi.org/10.3847/1538-4357/ad8570

Phan, T. D., Paschmann, G., Baumjohann, W., Sckopke, N., & Lühr, H. (1994). The magnetosheath region adjacent to the dayside magnetopause: Ampte/irm observations. *Journal of Geophysical Research*, *99*(A1), 121–141. https://doi.org/10.1029/93JA02444

Pitňa, A., Šafránková, J., Němeček, Z., Ďurovcová, T., & Kis, A. (2021). Turbulence upstream and downstream of interplanetary shocks. *Frontiers in Physics*, *8*, 654. https://doi.org/10.3389/fphy.2020.626768

Plaschke, F., Hietala, H., & Angelopoulos, V. (2013). Anti-sunward high-speed jets in the subsolar magnetosheath. *Annales Geophysicae*, *31*(10), 1877–1889. https://doi.org/10.5194/angeo-31-1877-2013

Plaschke, F., Hietala, H., Archer, M., Blanco-Cano, X., Kajdič, P., Karlsson, T., et al. (2018). Jets downstream of collisionless shocks. *Space Science Reviews*, *214*(5), 81. https://doi.org/10.1007/s11214-018-0516-3

Preisser, L., Blanco-Cano, X., Kajdič, P., Burgess, D., & Trotta, D. (2020). Magnetosheath jets and plasmoids: Characteristics and formation mechanisms from hybrid simulations. *The Astrophysical Journal Letters*, *900*(1), L6. https://doi.org/10.3847/2041-8213/abad2b

Preisser, L., Blanco-Cano, X., Trotta, D., Burgess, D., & Kajdič, P. (2020). Influence of He^{++} and shock geometry on interplanetary shocks in the solar wind: 2D hybrid simulations. *Journal of Geophysical Research: Space Physics*, *125*(4), e27442. https://doi.org/10.1029/2019JA027442

Price, C. P., Swift, D. W., & Lee, L. C. (1986). Numerical simulation of nonoscillatory mirror waves at the Earth's magnetosheath. *Journal of Geophysical Research*, *91*(A1), 101–112. https://doi.org/10.1029/JA091iA01p00101

Raptis, S., Karlsson, T., Plaschke, F., Kullen, A., & Lindqvist, P. (2020). Classifying magnetosheath jets using MMS: Statistical properties. *Journal of Geophysical Research: Space Physics*, *125*(11), e2019JA027754. https://doi.org/10.1029/2019JA027754

Raptis, S., Karlsson, T., Vaivads, A., Lindberg, M., Johlander, A., & Trollvik, H. (2022). On magnetosheath jet kinetic structure and plasma properties. *Geophysical Research Letters*, *49*(21), e2022GL100678. https://doi.org/10.1029/2022GL100678

Raptis, S., Karlsson, T., Vaivads, A., Pollock, C., Plaschke, F., Johlander, A., et al. (2022). Downstream high-speed plasma jet generation as a direct consequence of shock reformation. *Nature Communications*, *13*(1), 598. https://doi.org/10.1038/s41467-022-28110-4

Richardson, I. G., & Cane, H. V. (2010). Near-Earth interplanetary coronal mass ejections during solar cycle 23 (1996 - 2009): Catalog and summary of properties. *Solar Physics*, *264*(1), 189–237. https://doi.org/10.1007/s11207-010-9568-6

Schwartz, S. J., Burgess, D., & Moses, J. J. (1996). Low-frequency waves in the Earthś magnetosheath: Present status. *Annales Geophysicae*, *14*(11), 1134–1150. https://doi.org/10.1007/s00585-996-1134-z

Sckopke, N., Paschmann, G., Bame, S. J., Gosling, J. T., & Russell, C. T. (1983). Evolution of ion distributions across the nearly perpendicular bow shock: Specularly and non-specularly reflected-gyrating ions. *Journal of Geophysical Research*, *88*(A8), 6121–6136. https://doi.org/10.1029/JA088iA08p06121

Sckopke, N., Paschmann, G., Brinca, A. L., Carlson, C. W., & Luehr, H. (1990). Ion thermalization in quasi-perpendicular shocks involving reflected ions. *Journal of Geophysical Research*, *95*(A5), 6337–6352. https://doi.org/10.1029/JA095iA05p06337

Shaikh, Z. I., Raghav, A. N., & Vasko, I. Y. (2023). Proton Temperature Anisotropy within the Interplanetary Coronal Mass Ejections Sheath at 1 au. *The Astrophysical Journal Letters*, *955*(1), L5. https://doi.org/10.3847/2041-8213/acf575

Shue, J.-H., Song, P., Russell, C. T., Steinberg, J. T., Chao, J. K., Zastenker, G., et al. (1998). Magnetopause location under extreme solar wind conditions. *Journal of Geophysical Research*, *103*(A8), 17691–17700. https://doi.org/10.1029/98JA01103

Soucek, J., Escoubet, C. P., & Grison, B. (2015). Magnetosheath plasma stability and ulf wave occurrence as a function of location in the magnetosheath and upstream bow shock parameters. *Journal of Geophysical Research: Space Physics*, *120*(4), 2838–2850. https://doi.org/10.1002/2015JA021087

Soucek, J., Lucek, E., & Dandouras, I. (2008). Properties of magnetosheath mirror modes observed by Cluster and their response to changes in plasma parameters. *Journal of Geophysical Research*, *113*(A4), 2007JA012649. https://doi.org/10.1029/2007JA012649

Suni, J., Palmroth, M., Turc, L., Battarbee, M., Cozzani, G., Dubart, M., et al. (2023). Local bow shock environment during magnetosheath jet formation: Results from a hybrid-Vlasov simulation. *Annales Geophysicae*, *41*(2), 551–568. https://doi.org/10.5194/angeo-41-551-2023

Suni, J., Palmroth, M., Turc, L., Battarbee, M., Johlander, A., Tarvus, V., et al. (2021). Connection between foreshock structures and the generation of magnetosheath jets: Vlasiator results. *Geophysical Research Letters*, *48*(20), e2021GL095655. https://doi.org/10.1029/2021GL095655

Svenningsson, I., Yordanova, E., Khotyaintsev, Y. V., André, M., & Cozzani, G. (2025). Classifying the magnetosheath using local measurements from mms. *Journal of Geophysical Research: Space Physics*, *130*(1), e2024JA033272. https://doi.org/10.1029/2024JA033272

Svenningsson, I., Yordanova, E., Khotyaintsev, Y. V., André, M., Cozzani, G., & Steinvall, K. (2024). Whistler waves in the quasi-parallel and quasi-perpendicular magnetosheath. *Journal of Geophysical Research: Space Physics*, *129*(6), e2024JA032661. https://doi.org/10.1029/2024JA032661

Temmer, M. (2021). Space weather: The solar perspective. *Living Reviews in Solar Physics*, *18*(1), 4. https://doi.org/10.1007/s41116-021-00030-3

Treumann, R. A. (2009). Fundamentals of collisionless shocks for astrophysical application, 1. Non-relativistic shocks. *Astronomy and Astrophysics Review*, *17*(4), 409–535. https://doi.org/10.1007/s00159-009-0024-2

Verscharen, D., Chandran, B. D. G., Klein, K. G., & Quataert, E. (2016). Collisionless isotropization of the solar-wind protons by compressive fluctuations and plasma instabilities. *The Astrophysical Journal*, *831*(2), 128. https://doi.org/10.3847/0004-637X/831/2/128

Verscharen, D., Klein, K. G., & Maruca, B. A. (2019). The multi-scale nature of the solar wind. *Living Reviews in Solar Physics*, *16*(1), 5. https://doi.org/10.1007/s41116-019-0021-0

Vuorinen, L., Hietala, H., LaMoury, A. T., & Plaschke, F. (2023). Solar wind parameters influencing magnetosheath jet formation: Low and high IMF cone angle regimes. *Journal of Geophysical Research: Space Physics*, *128*(10), e2023JA031494. https://doi.org/10.1029/2023JA031494

Vuorinen, L., Hietala, H., & Plaschke, F. (2019). Jets in the magnetosheath: IMF control of where they occur. *Annales Geophysicae*, *37*(4), 689–697. https://doi.org/10.5194/angeo-37-689-2019

Vuorinen, L., LaMoury, A. T., Hietala, H., & Koller, F. (2023). Magnetosheath jets over solar cycle 24: An empirical model. *Journal of Geophysical Research: Space Physics*, *128*(8), e2023JA031493. https://doi.org/10.1029/2023JA031493

Walsh, B. M., Sibeck, D. G., Wang, Y., & Fairfield, D. H. (2012). Dawn-dusk asymmetries in the earth's magnetosheath. *Journal of Geophysical Research*, *117*(A12). https://doi.org/10.1029/2012JA018240

Xirogiannopoulou, N., Goncharov, O., Šafránková, J., & Němeček, Z. (2024). Characteristics of foreshock subsolar compressive structures. *Journal of Geophysical Research: Space Physics*, *129*(2), e2023JA032033. https://doi.org/10.1029/2023JA032033

Xu, F., & Borovsky, J. E. (2015). A new four-plasma categorization scheme for the solar wind. *Journal of Geophysical Research: Space Physics*, *120*(1), 70–100. https://doi.org/10.1002/2014JA020412

Yordanova, E., Vörös, Z., Raptis, S., & Karlsson, T. (2020). Current sheet statistics in the magnetosheath. *Frontiers in Astronomy and Space Sciences*, *7*, 2. https://doi.org/10.3389/fspas.2020.00002

Zhang, H., Zong, Q., Connor, H., Delamere, P., Facskó, G., Han, D., et al. (2022). Dayside transient phenomena and their impact on the magnetosphere and ionosphere. *Space Science Reviews*, *218*(5), 40. https://doi.org/10.1007/s11214-021-00865-0

Zhang, Y., Sun, T., Wang, C., Ji, L., Carter, J. A., Sembay, S., et al. (2022). Solar wind charge exchange soft x-ray emissions in the magnetosphere during an interplanetary coronal mass ejection compared to its driven sheath. *The Astrophysical Journal Letters*, *932*(1), L1. https://doi.org/10.3847/2041-8213/ac7521